Journal of Geochemical Exploration 196 (2019) 282–296

Contents lists available at ScienceDirect

Journal of Geochemical Exploration

journal homepage: www.elsevier.com/locate/gexplo

Ni-Co enrichment and High-Tech metals geochemistry in the Wingellina Ni-Co oxide-type laterite deposit (Western Australia)

F. Putzolu[a,*], M. Boni[a], N. Mondillo[a], M. Maczurad[b], F. Pirajno[c]

[a] Dipartimento Scienze della Terra Università di Napoli "Federico II" Complesso Universitario di Monte S. Angelo, Via Cintia 26 80126, Napoli, Italy
[b] Metals X Limited, L5/197 St Georges Terrace, Perth, WA, 6000, Australia
[c] Centre for Exploration Targeting, The University of Western Australia, 35, Stirling Highway, Crawley, WA 6009, Australia

ARTICLE INFO

Keywords:
Ni-Co laterite
Geochemistry
Rare Earth Elements
Scandium
Wingellina
Western Australia

ABSTRACT

The aim of this study is to evaluate the Ni-Co enrichment and the high-tech metals (REE and Sc) geochemistry in the Wingellina Ni-Co oxide-type laterite deposit (Western Australia). The study has been carried out on two mineralized cores (WPDD0012 and WPDD0019 drillcores) originating from two areas of the deposit. The geochemical assessments have been integrated with the analysis of laterite facies and sample mineralogy. In both the studied laterite profiles Ni enrichment was mostly controlled by the paragenetic evolution of the laterite itself, whereas Co enrichment was related to the formation of Mn-oxy-hydroxide-rich horizons in the limonitic ore-body. Significant REEs concentrations (up to 890 ppm) have been observed within the limonite zones. The correlation between REEs and the major oxides shows a decoupling between Ce and the other REEs, likely reflecting either a variable enrichment process among the different REEs, or a heterogeneous mineralogy of the REEs-bearing phases. Differently from other Ni-Co laterite deposits, Sc is only in limited part correlated with Fe_2O_3, having been most commonly detected in Ni- and SiO_2-rich zones of the saprolitic parts of the profiles. All the geochemical features, the facies characteristics and the Ni-Co, REEs and Sc grades observed in the two studied profiles seems to be the results of the interactions between two main controlling factors: distinct parent rock lithology and diverse degree of serpentinization.

1. Introduction

Ni-laterites play a primary role in the nickel industry, accounting for about 70% of the world's Ni resources (Butt and Cluzel, 2013), as well as for about 20% of the world's cobalt production. It is well known that the majority of the cobalt production originates from the so-called "high-risk" countries, such as the Democratic Republic of the Congo, which for example accounts for 50% of the Co global production (Kapusta, 2006). Therefore, studies on the Co mineralogical and geochemical deportment and on its spatial distribution within Ni-laterites are crucial in order to unlock thousands of tonnes of Co reserves in more geopolitically stable countries.

In addition, since the rapid growth in demand for the so-called "High-Tech metals" (e.g. Chakhmouradian and Wall, 2012), Ni-Co laterites are also considered worthy targets for exploration of elements such as Rare Earth Elements and Scandium (e.g. Economou-Eliopoulos et al., 1997; Eliopoulos and Economou-Eliopoulos, 2000; Audet, 2008; Aiglsperger et al., 2015, 2016).

Lateritic nickel and cobalt deposits result from the chemical weathering of mafic to ultramafic protoliths at tropical to sub-tropical latitudes (e.g. Gleeson et al., 2003; Freyssinet et al., 2005; Golightly, 2010). On the basis of the most abundant Ni-bearing mineralogical association, these deposits are classified as oxide-type or silicate-type (Brand et al., 1998; Freyssinet et al., 2005). In general, oxide-type laterites occur in stable tectonic terranes and in zones of low relief. These settings promote the high-standing of the water table and the direct precipitation of ore-bearing (hydr)oxides from the chemical leaching of Ni-bearing olivine and of other ferromagnesian minerals. According to this model, the residual enrichment of Ni and Fe (+Co and Mn) enhances the formation of a well-developed ferruginous unit, called limonite zone, and of a thin saprolite horizon (Butt and Cluzel, 2013). In contrast, silicate-rich ores are associated with a multi-stage development, marked by syn-tectonic weathering processes, which are typical of active margins. In this framework, the uplift of the regolith profiles causes the lowering of the water table and hence the leaching of Ni from the upper limonite and its capture by secondary silicate phases (i.e. hydrous Mg-silicates) in the lower saprolite (Freyssinet et al., 2005; Golightly, 2010; Butt and Cluzel, 2013).

* Corresponding author.
E-mail address: francesco.putzolu@unina.it (F. Putzolu).

https://doi.org/10.1016/j.gexplo.2018.11.004
Received 27 March 2018; Received in revised form 24 October 2018; Accepted 6 November 2018
Available online 11 November 2018

The Wingellina orebody (Metals X Limited owned property), in Western Australia is part of the Central Musgrave Project and is one of the Australia's largest undeveloped Ni-Co laterite deposit. The project encloses a Probable Mining Reserve of 168 Mt. of limonitic ore grading 0.98% Ni and 0.08% Co (Metals X Ltd, 2017). The aim of this study is to evaluate the geochemistry of two mineralized drillcores, characterized by distinct mineralogy (one is limonite-prevailing, whereas the other is saprolite-prevailing) from the Wingellina deposit, to better constrain the behavior of the major elements plus Ni and Co, in relationship with facies and mineralogical variations in the laterite profiles. A particular emphasis has been given to the assessment of the main ore-forming processes that accounted for the development of a variable range of facies within the laterite profiles, and to the mineral deportment of REEs and Sc, which could represent potential by-products of Ni and Co extraction.

2. Geological background

2.1. Regional geology

The Wingellina Ni-Co laterite deposit occurs within the Musgrave Province (Fig. 1a, b), which is an east-trending Proterozoic orogenic belt lying at the nexus of the Australia's three cratonic provinces (West, North, and South Australian Cratons, Fig. 1a) (Howard et al., 2015). The Wingellina ore-bearing laterite is derived from the weathering of the Wingellina Hill mafic to ultramafic layered intrusion (i.e. Hinckley Range Gabbro Formation), which is part of the Mesoproterozoic Warakurna Large Igneous Province (Wingate et al., 2004; Pirajno and Hoatson, 2012) and the 1085–1040 Ma Giles Event (Maier et al., 2014, 2015). These mafic to ultramafic intrusions, called Giles Complex Suite (Maier et al., 2014, 2015), were emplaced in a Paleoproterozoic basement consisting of high-grade granulite facies gneisses (i.e. Musgravian Gneisses) (Nesbitt et al., 1970; Major and Conor, 1993; Camacho and Fanning, 1995; Edgoose et al., 2004). Maier et al. (2014 and 2015) classified the intrusive bodies of the Giles Suite into several types: ultramafic intrusions (e.g. Wingellina Hills), gabbroic intrusions, anorthosite and troctolitic intrusions. The coeval lithologies of the Bentley Supergroup and the Tjauwata Group represent the volcanic products and subordinate rift sediments related to the magmatism of the Giles event (Sun et al., 1996).

The most recent (0.63–0.53 Ga) tectonic event that shaped the Musgrave Province is the Petermann Orogeny (Camacho et al., 1997; Camacho and McDougall, 2000). This orogeny triggered the exhumation in sub-aerial environment of the Musgrave Province (e.g. Hoskins and Lemon, 1995; Walter et al., 1995; Hand and Sandiford, 1999; Wade et al., 2005). In this tectonic framework, the Australia's weathering history has been variable and complex, with parts of the continent (e.g. Yilgarn Craton, Musgrave Province) that have experienced a subaerial exposure since the Precambrian (Anand and Paine, 2002). According to Pillans et al. (2005), the geochronology of the Australian regolith covers suggests that the whole Phanerozoic of the Australian continent has been characterized by several stages of warm and humid climatic conditions, which enhanced the intensive weathering and alteration of the exposed rocks. The Quaternary (Late Miocene or Pliocene) shift to more arid to semi-arid conditions played an important control on the evolution experienced by Australia's regolith (Tardy and Roquin, 1998; Anand and Paine, 2002). However, in the specific case of the Musgrave Province, it must be highlighted that the age of the weathering event associated with the Wingellina lateritization process still remains undefined.

2.2. Local geology

The Wingellina laterite profile derives from the weathering of the layered mafic to ultramafic intrusion of the Wingellina Hills (Giles Suite). This intrusion occurs as a southeast-trending and southwest-dipping mafic-ultramafic set of ridges (Fig. 2), which are deformed by several south-easterly trending shear- and mylonitic zones and by east-west trending brittle cross-structures. According to Ballhaus and Glikson (1989) the magmatic sequence at Wingellina consists of several ultramafic units, which start with a basal orthopyroxenite, followed by a clinopyroxenite and peridotite (olivine-spinel cumulate) and by a wehrlite, whereas the shallower and relatively fractionated products are mainly gabbro and gabbronorite units. The Wingellina lateritic orebody is located in elongated valleys, which have a sub-parallel trend to the shear- and mylonitic zones affecting the magmatic bedrock. This feature suggests that the pre-weathering deformation of the intrusion played an important role in defining the optimal drainage and topographic conditions that may have locally improved the weathering degree and the preservation of the lateritic profile respectively.

In general, the typical Wingellina profile (laterite sensu stricto; *s.s.*) displays the following zones from top to the bottom: carbonate-rich duricrust, (hydr)oxide-rich limonite, silicate-rich saprolite, and magmatic bedrock. In contrast, the central sector of the tenure (Fig. 2) is occupied by a thick silica- and magnesite-rich unit, called “jasperoid laterite”. This facies is crosscut by pale green chrysoprase veins and lies above poorly serpentinized dunite and peridotite units. The exploitable Ni and Co resources are associated with the (hydr)oxide-rich limonite zone, which is the best developed horizon of the laterite *s.s.* and has an average thickness of about 80 m. The two cores selected for this study, though both related to the laterite *s.s.*, display remarkable differences in their profiles (Figs. 2, 3 and 4).

3. Description of the cores, sampling and analytical methods

This study was carried out on two mineralized drillcores (WPDD0012 and WPDD0019) drilled by the Metals X Ltd in 2007 in the high-grade zone of the laterite *s.s.* (Fig. 2).

3.1. Drillcore WPDD0012

The core WPDD0012 (7117583N; 497093E; Dip: −60; Azimuth: 49) was drilled in the southern zone of the deposit (Fig. 2), and reached a depth of 78.6 m (Fig. 3a). In the uppermost zone of the drillhole (0–2 m) the duricrust occurs as a reddish and relatively indurated unit crosscut by veinlets of carbonates and Fe-(hydr)oxides (Fig. 3b). The limonite zone occurring in this core is intercepted at depths of between 2 and 72 m, and therefore is the most developed unit. This unit consists of a brittle and fine-grained lithotype, locally characterized by disseminated (Fig. 3c) or massive Mn-(hydr)oxides (Fig. 3d). Within the same limonite unit (Fig. 3a), several clay-rich mottled horizons occur between 36 and 45 m and 68 to 72 m in depth. From 72 to 76 m depth, the core comprises the silicates-rich saprolite zone, which consists of a massive, bright green lithology locally spotted by reddish to black coatings of Fe-(hydr)oxides (Fig. 3f). The bottom part of the drillcore intercepts the local magmatic bedrock corresponding to relatively unweathered gabbro/gabbronorite (Fig. 3g).

3.2. Drillcore WPDD0019

The core WPDD0019 (7117900N; 495336E; Dip: −60; Azimuth: 49) was drilled in the north-western sector of the southern zone of the tenentment (Fig. 2) and reaches a depth of 56.8 m. In comparison to the other analyzed core (WPDD0012), here the lateritic profile has a better developed silicate-rich saprolite, whereas the residual (hydr)oxide zone is only subordinate (Fig. 4a). The surficial zone of the weathering profile (0–2.5 m) is occupied by the silica- and carbonate-rich duricrust (Fig. 4b), which is characterized by a higher cementation degree compared to that of the other drillcore (WPDD0012). In addition, the duricrust in this locality is characterized by the occurrence of nodular carbonates and by sub-angular and silicified limonite fragments, all of this suggesting a partial reworking of the regolith profile (Fig. 4b). The

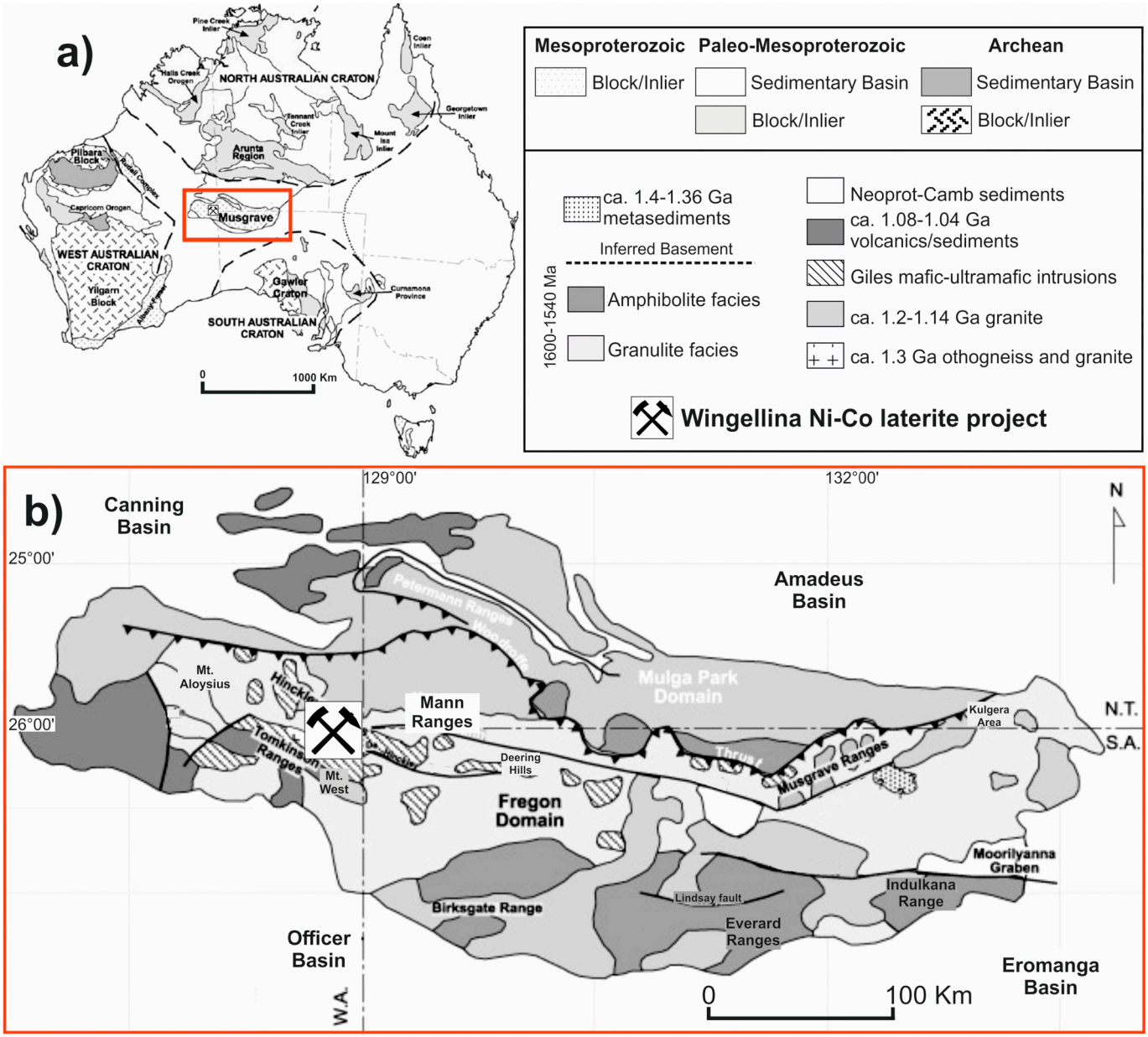

Fig. 1. a) Map of the Australian continent displaying the locations of Archaean cratons and Palaeo-Mesoproterozoic terrains (after Wade et al., 2006 modified). The rectangle highlights the position of Musgrave Province, displayed in Fig. 1b. b) Geology of the Musgrave Province (after Wade et al., 2006 modified) showing the location of the Wingellina Ni-Co laterite deposit.

limonite zone starts at a depth of 2.5 m and continues down to 25 m; this zone is locally coated by pseudo-layered Mn-(hydr)oxides and by microcrystalline carbonates (Fig. 4c). The core intersects the silicates-rich saprolite horizon between 25 and 55.5 m in depth. In this zone the saprolite unit has different features compared to the saprolite zone in core WPDD0012. In particular, the uppermost portion of the saprolite unit (25 to 45 m, Fig. 4d) consists of brownish clays, locally crosscut by pale green silicate-rich veins associated with a silica boxwork (Fig. 4e). The lower saprolite (45 to 55 m in depth, Fig. 4f and g) occurs as a waxy and pale green unit. In this zone, carbonate veins are common (Fig. 4f). In the lowermost saprolite interval (54.5 m in depth), carbonates occur as partially oxidized microcrystalline nodules (Fig. 4h). At the bottom of the core, several green and dense saprock blocks, likely corresponding to relicts of serpentinized peridotites, are cemented by saprolitic silicates (Fig. 4i).

3.3. Sampling and methods

For the present study 31 core samples were collected from drillcores WPDD0012 (18 samples) and WPDD0019 (13 samples). The down hole sample positions are shown in Figs. 3a and 4a. The adopted sampling strategy was aimed primarily to best represent the lithological, facies and textural variability of the identified horizons within the laterite profiles.

The chemical analyses of major, minor and trace elements on the core samples were carried out at the Bureau Veritas Laboratory in Canada. Prior to the analyses, the samples were prepared through drying at 105 °C. For the major and minor element determinations, 0.5 g of pulp has been leached with “aqua regia” and then flux fused with $LiBO_2/Li_2B_4O_7$ for Inductively Coupled Plasma Emission Spectrometry (ICP-ES) analyses. Major oxides and minor elements have been analyzed with a Method Detection Limit (MDL) between 0.01 and

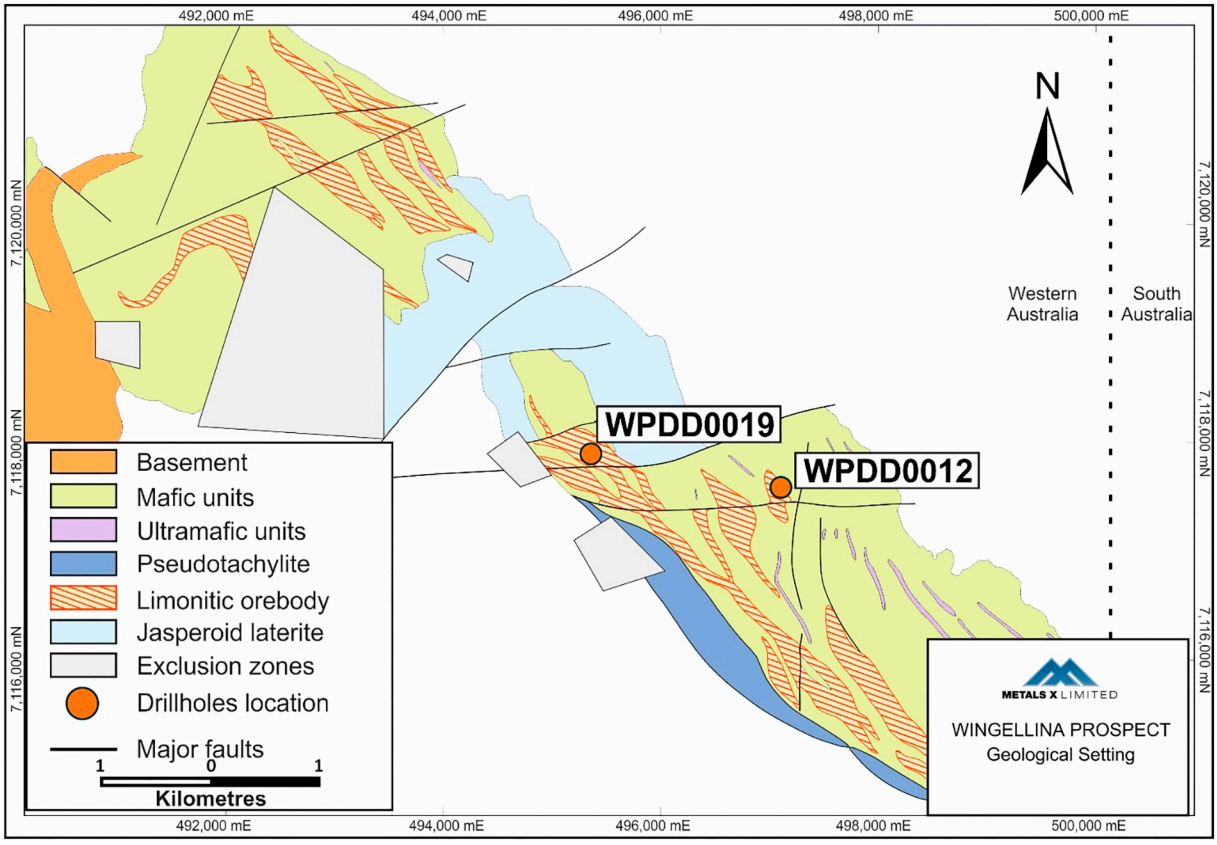

Fig. 2. Geological map of the Wingellina Ni-Co laterite deposit, including the location of the studied drillcores (after Putzolu et al., 2018, modified).

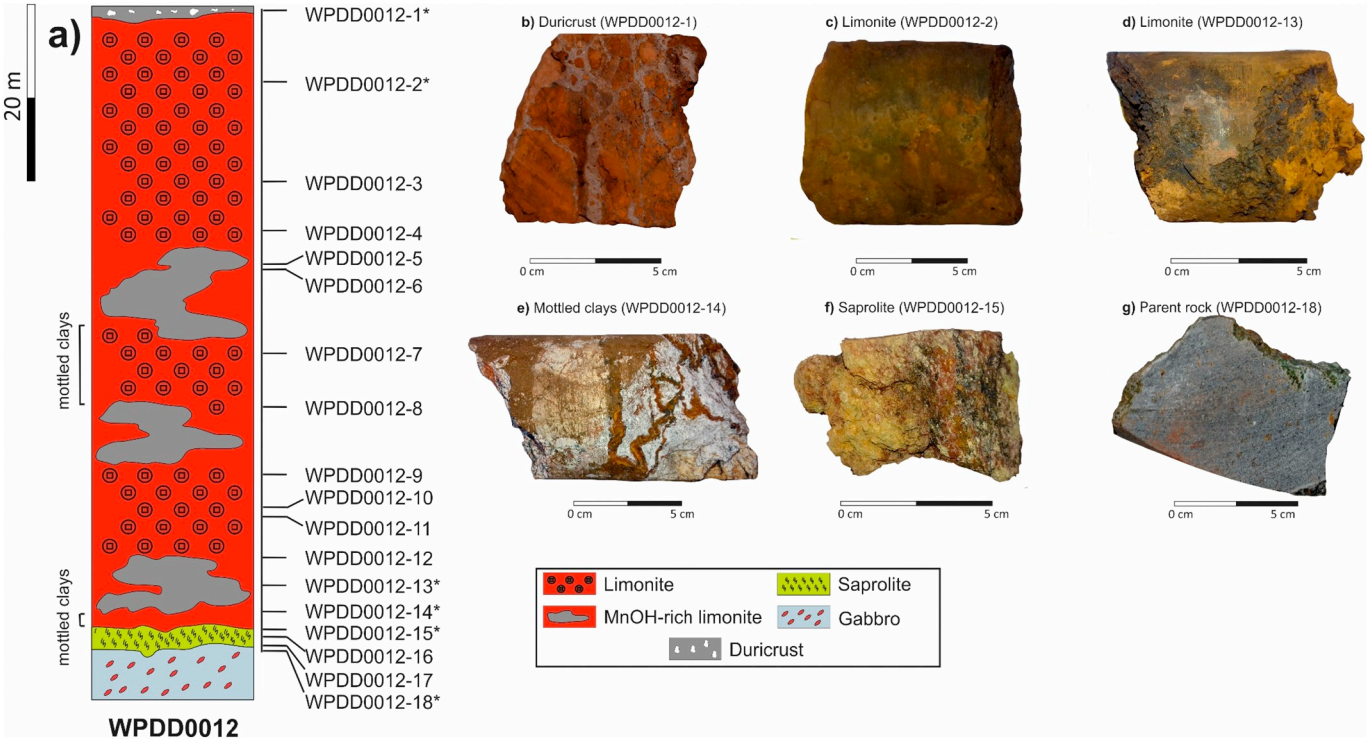

Fig. 3. Wingellina lateritic profile at the drilling site WPDD0012 and images of representative specimens. a) Stratigraphic column based on drillhole WPDD0012 showing the core samples locations (after Putzolu et al., 2018, modified); b) Duricrust sample (depth: 0.5 m); c) and d) Manganesiferous limonite samples (depth: 9 and 68 m respectively); e) Mottled clays sample (depth: 71.2 m); f) Saprolite sample (depth: 73 m) g) Parent rock sample (depth: 75.8 m). The asterisk indicates the position of the displayed representative samples.

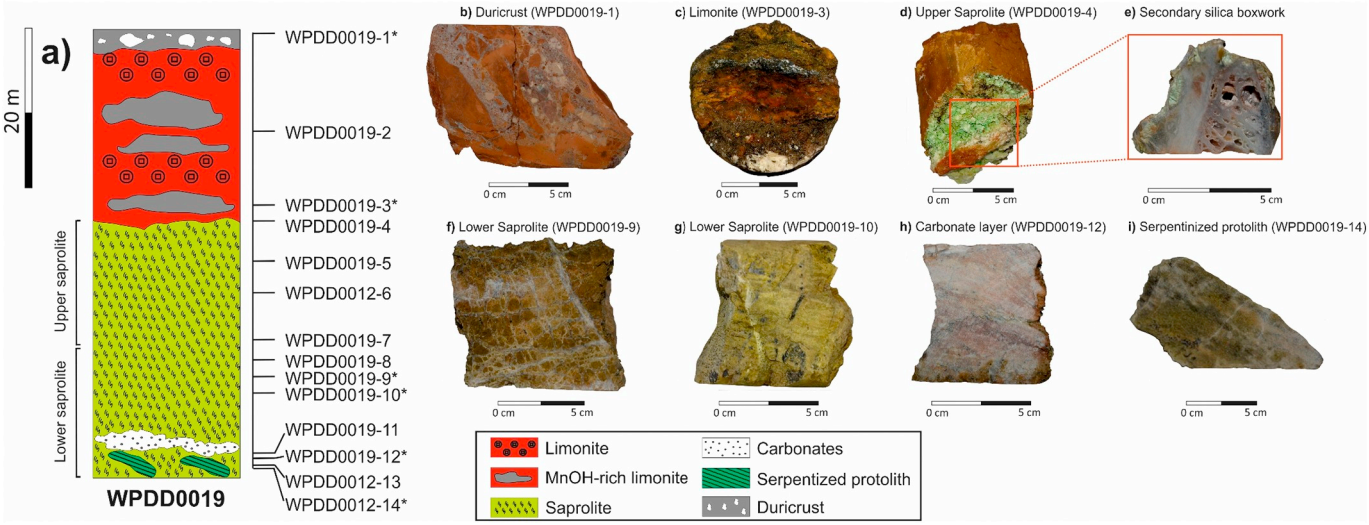

Fig. 4. Wingellina lateritic profile at the drilling site WPDD0019 and images of representative specimens. a) Stratigraphic column based on drillhole WPDD0019 (after Putzolu et al., 2018, modified) showing the core samples locations; b) Duricrust sample (depth: 1.6 m); c) Manganesiferous limonite samples (depth: 23 m); d) saprolite sample (depth: 25 m) e) silica-rich boxwork within the saprolite sample WPDD0019.4; f) and g) saprolite sample (depth: 44.5 and 46.5 m respectively); h) carbonate pod sample (depth: 54.5 m); i) serpentinized parent rock sample (depth: 56 m). The asterisk indicates the position of the displayed representative samples. N.B.: the carbonate sample WPDD0019-12 (drillcore WPDD0019) is not included in the geochemical analyses.

0.001 wt%. Loss on ignition (LOI) has been evaluated at 1000 °C, with a MDL of −5.1 wt%. Trace element determinations (including REEs, Sc) have been carried undertaken by Inductively Coupled Plasma Mass Spectrometry (ICP-MS), with a MDL between 0.01 and 8 ppm. Finally, Nickel, Cobalt and Copper have been analyzed with acid digestion through IPC-ES with a MDL of 0.001 wt%.

4. Results

4.1. Major oxides composition and the Ni-Co grades

The geochemical data of major, minor and trace elements of drillcores WPDD0012 and WPDD0019 are summarized in Tables 1 and 2 respectively.

4.1.1. Drillcore WPDD0012

Fig. 5a shows the geochemical trends observed in the lateritic profile of the core WPDD0012 (from sample 12-1 to sample 12-18). The dominant oxides are Fe_2O_3, SiO_2 and Al_2O_3, with average values of 35.61, 21.61 and 16.38 wt%. Fe_2O_3 has an increasing trend from the weathered gabbro bedrock (WPDD0012-18) to the uppermost zone of the limonite, whereas it shows a sharp decrease in correspondence of the mottled clays horizons (WPDD0012-8, WPDD0012-9 and WPDD0012-11) and in the duricrust (WPDD0012-1). SiO_2 and Al_2O_3 have both inverted tendencies compared to Fe_2O_3. In particular, SiO_2 undergoes a slight increase from the gabbro to the saprolite horizon, where it reaches its highest values (55.38 wt% SiO_2, WPDD0012-17). Silica then remains very low throughout the limonite zone, except for the mottled clays horizons from 25.62 and 34.53 wt% SiO_2. In addition, a SiO_2 increase has been observed also in the duricrust (8.18 wt%). The geochemical trend is quite irregular for Al_2O_3, whose values decrease from the gabbro (WPDD0012-18, 11.81 wt%) to the duricrust (WPDD0012-1, 4.39 wt%). Al_2O_3 reaches the highest content in limonite samples (up to 33.29 wt% in WPDD0012-7). In addition, the Al_2O_3 trend from the gabbro bedrock to the mottled clay sample WPDD0012-8 is similar to that of SiO_2, whereas in the uppermost zone of the profile this correlation is not observed.

MgO and CaO have similar trends, characterized by sharply decreasing concentrations from the bottom gabbro (WPDD0012-18) to the upper limonite zone (WPDD0012-2), and by a sharp increase in the duricrust (sample WPDD0012-1). Differently from CaO, in the saprolite zone (samples WPDD0012-17 to WPDD0012-15) MgO has still remarkably high values (average 4.64 wt%), which rapidly drop the at the interface with the limonite zone (WPDD0012-14, 0.64 wt%).

MnO shows negligible concentration values both in the gabbro (WPDD0012-18, 0.09 wt% MnO) and in the saprolite zone (WPDD0012-15 to WPDD0012-17, average value: 0.40 wt%), whereas it is significantly enriched within the limonite, with average values of 4.00 wt %. The MnO concentration strongly decreases in the duricrust (0.36 wt %). The Co-grade generally increases from the gabbro (WPDD0012-18, 0.003 wt% Co) to the limonite, where it reaches its highest average values (0.37 wt% Co), and sharply decreases in the duricrust (WPDD0012-1,0.025 wt%). The Co trend within the limonite is very similar to that of MnO.

Nickel shows a rapid increase in the transition zone from the gabbro (WPDD0012-18, 0.07 wt%) to the saprolite, where a sharp positive peak could be observed (WPDD0012-16, 3.33 wt%). Nickel displays a relative decrease in the limonite zone, with average values of 1.24 wt%. The duricrust sample has a Ni content of 0.50 wt%. The Ni trend is quite variable and is generally correlated to the abundance of MnO (and thus of Co) within the limonite, whereas in the saprolite zone a SiO_2-Ni geochemical association is far more evident.

4.1.2. Drillcore WPDD0019

The major and minor chemical compositions measured along the core WPDD0019 are shown in Fig. 5b (19-1 to 19-14). Compared to the core WPDD0012, in this case a sharp enrichment of SiO_2 and MgO (average values: 30.16 and 13.45 wt% respectively) and a depletion of Fe_2O_3 and Al_2O_3 (average values: 19.32 and 4.40 wt% respectively) have been observed.

Silica undergoes a strong increase in the transition from the gabbro (WPDD0019-14, 8.33 wt%) toward the saprolite, where it reaches its highest values (WPDD0019-4 to WPDD0019-13, average value: 37.83 wt%), even though with an irregular trend. In the limonite zone (WPDD0019-2 to WPDD0019-3) the SiO_2 amount decreases, however still maintaining remarkably high values (average value: 18 wt%) if compared to those of the uppermost zone of core WPDD0012, whereas SiO_2 in the duricrust (WPDD0019-1) decreases to values of 7.23 wt% SiO_2. Fe_2O_3 sharply increases from the parent rock (5.38 wt%) to the saprolite horizon (where it averages 18.47 wt%). In this zone of the

Table 1
Chemical composition of the laterite profile of drillcore WPDD0012.

	Sample ID	WPD-D0012-1	WPD-D0012-2	WPD-D0012-3	WPD-D0012-4	WPD-D0012-5	WPD-D0012-6	WPD-D0012-7	WPD-D0012-8	WPD-D0012-9	WPD-D0012-10	WPD-D0012-11	WPD-D0012-12	WPD-D0012-13	WPD-D0012-14	WPD-D0012-15	WPD-D0012-16	WPD-D0012-17	WPD-D0012-18
	Unit*	D	L	L	L	L	L	L	L	L	L	L	L	L	L	S	S	S	P
SiO_2	wt%	8.18	2.22	2.70	3.05	3.56	3.50	16.07	30.53	34.83	10.28	25.62	11.21	4.38	31.81	46.46	49.50	55.38	49.70
Al_2O_3	wt%	4.39	4.76	19.59	19.20	19.02	18.50	33.29	26.42	29.26	8.43	20.77	9.25	5.14	25.08	13.61	10.60	15.76	11.81
Fe_2O_3	wt%	16.57	64.02	54.70	54.48	53.99	55.65	25.95	23.99	12.55	60.18	30.28	54.49	58.38	24.56	21.72	18.12	7.03	4.34
MgO	wt%	12.00	1.24	0.99	0.77	0.83	0.68	0.67	0.42	0.69	1.08	1.08	0.80	0.63	0.64	3.24	4.45	6.25	14.53
CaO	wt%	21.86	0.35	0.07	0.06	0.08	0.07	0.05	0.06	0.09	0.07	0.11	0.12	0.20	0.07	0.25	0.32	0.51	17.68
Na_2O	wt%	0.09	0.51	0.12	0.04	0.18	0.10	0.07	0.10	0.15	0.05	0.10	0.07	0.05	0.07	0.12	0.17	0.15	0.52
K_2O	wt%	0.12	0.07	< 0.01	< 0.01	< 0.01	< 0.01	< 0.01	0.02	0.03	< 0.01	0.02	< 0.01	0.11	< 0.01	< 0.01	0.02	0.02	< 0.01
TiO_2	wt%	0.24	0.34	0.24	0.28	0.27	0.20	1.52	3.43	0.36	0.29	0.86	0.24	0.07	0.10	0.39	0.31	0.14	0.10
P_2O_5	wt%	0.01	< 0.01	< 0.01	< 0.01	0.02	0.02	0.20	0.15	< 0.01	< 0.01	< 0.01	0.02	0.01	< 0.01	< 0.01	< 0.01	< 0.01	< 0.01
MnO	wt%	0.36	9.13	1.55	1.86	1.99	2.02	0.22	2.04	5.79	0.84	5.04	5.76	12.95	2.83	0.82	0.17	0.22	0.09
Cr_2O_3	wt%	0.97	0.56	0.43	0.64	0.27	0.35	2.65	0.17	0.25	4.13	0.26	0.54	0.55	0.09	1.18	2.75	1.05	0.39
Ni	wt%	0.50	2.10	0.83	1.24	1.14	1.21	0.33	0.43	1.21	1.07	1.80	2.10	1.78	0.95	2.13	3.33	2.10	0.07
Co	wt%	0.03	0.57	0.10	0.13	0.20	0.10	0.02	0.06	0.60	0.14	0.63	0.92	1.23	0.41	0.04	0.01	0.01	0.00
LOI	wt%	34.05	13.18	18.27	17.66	17.90	17.05	18.62	11.40	13.45	12.91	12.76	13.49	13.57	12.96	9.13	9.11	10.49	0.38
Sc	ppm	13	48	37	53	38	37	44	28	11	52	40	51	52	80	129	140	66	42
Cu	ppm	30	60	60	60	100	60	110	40	20	70	60	50	50	10	10	20	10	20
Nb	ppm	< 5	< 5	< 5	< 5	< 5	< 5	< 5	128	84	< 5	10	< 5	< 5	< 5	< 5	< 5	< 5	7
Ba	ppm	239	336	92	310	197	244	9	346	400	18	132	176	805	14	41	8	34	17
Be	ppm	< 1	< 1	< 1	< 1	< 1	< 1	< 1	2	< 1	< 1	< 1	< 1	< 1	< 1	< 1	< 1	< 1	< 1
Cs	ppm	< 0.1	< 0.1	< 0.1	< 0.1	< 0.1	< 0.1	< 0.1	< 0.1	< 0.1	< 0.1	< 0.1	< 0.1	< 0.1	< 0.1	< 0.1	< 0.1	< 0.1	< 0.1
Ga	ppm	4.3	20.7	14.7	17.8	16.7	18	28.6	35.8	59.7	15.1	23.8	16.6	16.8	13.4	10.8	8.8	6.8	7.7
Hf	ppm	3.5	0.4	0.2	0.3	0.4	0.2	3.4	75	2.6	0.4	1.9	0.4	0.1	< 0.1	0.5	0.4	0.2	0.1
Nb	ppm	1.7	< 0.1	< 0.1	< 0.1	< 0.1	< 0.1	8.5	129.2	87.6	0.4	8.7	0.2	< 0.1	< 0.1	< 0.1	< 0.1	< 0.1	0.8
Rb	ppm	3.9	1	< 0.1	< 0.1	0.3	0.1	0.6	1	1.7	0.8	0.8	0.4	1.7	< 0.1	0.7	1.3	0.8	< 0.1
Sr	ppm	933.8	126.1	15.3	19.6	23.3	39.3	11.4	47.6	32.6	12.3	46.1	67.6	290.9	25.7	46.8	41	47.8	53.7
Ta	ppm	0.1	< 0.1	< 0.1	< 0.1	< 0.1	< 0.1	0.5	6.4	4.7	< 0.1	0.6	< 0.1	< 0.1	< 0.1	< 0.1	< 0.1	< 0.1	< 0.1
Th	ppm	0.5	< 0.2	< 0.2	< 0.2	< 0.2	< 0.2	1	10.5	30.6	< 0.2	1.4	0.4	< 0.2	< 0.2	< 0.2	0.2	< 0.2	< 0.2
U	ppm	1.2	< 0.1	< 0.1	< 0.1	0.2	0.2	1.2	2.6	1.8	1.4	0.8	0.6	0.5	0.4	0.1	0.3	0.2	< 0.1
V	ppm	97	190	184	240	259	295	347	190	78	267	194	336	243	196	275	140	116	169
W	ppm	< 0.5	< 0.5	< 0.5	< 0.5	< 0.5	< 0.5	< 0.5	< 0.5	4.3	< 0.5	0.7	< 0.5	< 0.5	< 0.5	< 0.5	< 0.5	< 0.5	< 0.5
Zr	ppm	142	11.8	9	8.5	10.6	7.5	136.6	3073.9	49.6	12.5	54.5	11.2	4.9	2.2	11.5	9.5	6.3	3.4
Y	ppm	3.2	20.7	7.2	7.8	15.8	7.5	8.7	50.3	29.4	24.2	17.6	38.1	51.5	5.7	9	11.9	34.4	4.1
La	ppm	2	7.3	3.1	4.7	3.5	4.5	14.6	165.2	19.3	13.5	19.9	20	84	2.5	10.2	3.4	12	1.5
Ce	ppm	5.2	23.3	32.1	46.8	60.3	96.7	12.1	501.3	268.1	4.7	57.6	2.4	12.2	2.3	1.9	0.8	1.8	0.9
Pr	ppm	0.57	2.28	2.05	1.58	1.79	1.78	2.83	35.51	5.05	2.69	8.62	11.15	36.26	1.15	3.04	0.81	4.14	0.19
Nd	ppm	2.5	11	9.1	7.1	9	8.2	11.5	127.4	19.4	13.2	38.4	50	144.3	5	11.7	3.2	17	0.9
Sm	ppm	0.58	1.94	2.75	2.5	3.87	2.54	2.37	18.77	4.5	4.63	7.42	12.43	32.46	1.08	1.89	0.86	3.46	0.31
Eu	ppm	0.15	0.62	0.76	0.67	1.14	0.66	0.48	1.19	0.69	0.93	1.35	2.55	6.45	0.24	0.46	0.29	1.08	0.12
Gd	ppm	0.58	3.37	2.55	2.25	4.43	2.38	2.16	13.99	4.99	4.2	6.09	11.57	26.68	1.22	2.31	1.58	5.8	0.5
Tb	ppm	0.09	0.4	0.44	0.45	0.95	0.45	0.34	1.71	0.83	0.87	0.97	2.2	4.77	0.21	0.35	0.34	1.07	0.1
Dy	ppm	0.57	2.66	2.74	2.79	5.81	2.63	2.15	9.42	5.21	5.3	5.53	13.2	26.59	1.44	2.3	2.34	7.38	0.72
Ho	ppm	0.1	0.6	0.51	0.55	1.17	0.5	0.41	1.9	1.08	1.03	1.07	2.48	4.98	0.25	0.5	0.54	1.61	0.15
Er	ppm	0.34	1.48	1.42	1.64	3.53	1.46	1.29	5.97	3.26	3.11	2.98	6.92	13.13	0.75	1.36	1.75	4.67	0.45
Tm	ppm	0.05	0.14	0.15	0.24	0.47	0.22	0.19	0.96	0.49	0.5	0.44	0.98	1.75	0.09	0.18	0.25	0.55	0.05
Yb	ppm	0.43	0.82	1.01	1.57	2.29	1.25	1.39	7.18	2.99	3.55	2.61	5.53	9.56	0.51	1.06	1.64	3.2	0.31
Lu	ppm	0.05	0.11	0.13	0.21	0.35	0.18	0.2	1.23	0.46	0.5	0.41	0.83	1.35	0.07	0.16	0.27	0.51	0.05
REEs	ppm	13.21	56.02	58.81	73.05	98.60	123.45	52.01	891.73	336.35	58.71	153.39	142.24	404.48	16.81	37.41	18.07	64.27	6.25
Ce/Ce*		1.17	1.38	3.07	4.14	5.80	8.23	0.45	1.58	6.54	0.19	1.06	0.04	0.05	0.33	0.08	0.12	0.06	0.41
Eu/Eu*		0.75	0.70	0.83	0.82	0.79	0.77	0.61	0.21	0.42	0.61	0.58	0.61	0.63	0.60	0.64	0.72	0.70	0.88
UMIA		27.22	87.27	89.68	89.53	88.11	88.79	68.10	49.22	43.99	71.20	50.73	69.24	83.06	47.24	27.11	21.43	19.10	13.46

Unit abbreviations: D = duricrust; L = limonite; S = Saprolite; P = Protolith.

Table 2
Chemical composition of the laterite profile of drillcore WPDD0019.

	Sample ID	WPDD0019-1	WPDD0019-2	WPDD0019-3	WPDD0019-4	WPDD0019-5	WPDD0019-6	WPDD0019-7	WPDD0019-8	WPDD0019-9	WPDD0019-10	WPDD0019-11	WPDD0019-13	WPDD0019-14
	Unit*	D	L	L	S	S	S	S	S	S	S	S	S	S-P
SiO_2	wt%	7.23	6.47	29.53	62.87	39.82	28.72	44.38	38.16	11.88	40.72	29.23	44.73	8.33
Al_2O_3	wt%	1.18	6.09	2.28	2.97	5.98	9.34	6.62	5	2.02	3.87	4.61	6.44	0.85
Fe_2O_3	wt%	14.99	50.75	13.71	10.6	24.66	30.75	22.74	17.16	6.28	17.98	12.95	23.15	5.38
MgO	wt%	7.18	1.24	1.75	11.79	14.24	13.56	12.21	23.14	18.92	21.64	17.71	12.52	18.93
CaO	wt%	32.82	0.09	0.4	1.04	0.06	0.08	0.06	0.09	22.07	0.11	10.66	0.36	25.36
Na_2O	wt%	0.04	0.21	0.33	0.19	0.11	0.14	0.1	0.07	0.07	0.09	0.1	0.16	0.02
K_2O	wt%	0.09	0.14	0.4	0.02	< 0.01	< 0.01	< 0.01	< 0.01	< 0.01	< 0.01	< 0.01	< 0.01	< 0.01
TiO_2	wt%	0.17	0.08	0.07	0.05	0.13	0.13	0.09	0.05	0.02	0.08	0.05	0.08	0.02
P_2O_5	wt%	0.01	0.06	< 0.01	< 0.01	< 0.01	< 0.01	0.01	< 0.01	< 0.01	< 0.01	< 0.01	< 0.01	< 0.01
MnO	wt%	0.03	17.51	33.87	0.32	0.3	0.33	0.31	0.2	0.07	0.21	0.17	0.24	0.05
Cr_2O_3	wt%	0.377	0.25	0.35	0.613	1.507	1.859	1.417	0.969	0.545	1.245	0.85	1.422	0.385
Ni	wt%	0.203	1.28	2.8	1.89	2.6	3.1	2.3	2.6	0.566	2.4	0.347	0.686	0.135
Co	wt%	0.004	0.45	0.691	0.019	0.028	0.033	0.029	0.02	0.007	0.02	0.015	0.024	0.005
LOI	wt%	35.33	13.58	11.85	6.6	9.42	10.6	8.74	11.27	36.98	10.4	22.79	9.69	40.13
Sc	ppm	5	23	12	18	21	27	21	17	5	17	8	16	6
Cu	ppm	40	320	140	20	60	40	40	20	20	30	30	70	20
Nb	ppm	17	< 5	23	< 5	< 5	7	8	7	7	< 5	< 5	< 5	9
Ba	ppm	169	10,669	10,011	153	28	33	19	33	30	84	52	57	17
Be	ppm	< 1	< 1	< 1	< 1	< 1	< 1	< 1	< 1	< 1	< 1	< 1	< 1	< 1
Cs	ppm	< 0.1	0.3	1.9	< 0.1	< 0.1	< 0.1	< 0.1	< 0.1	< 0.1	< 0.1	< 0.1	< 0.1	< 0.1
Ga	ppm	2	17	26.4	13.5	10.7	10.3	7.9	5.8	1.6	4.1	3.5	4.9	< 0.5
Hf	ppm	2.4	0.1	< 0.1	< 0.1	0.1	0.2	0.1	< 0.1	< 0.1	< 0.1	< 0.1	< 0.1	< 0.1
Nb	ppm	2.2	< 0.1	< 0.1	0.8	0.1	< 0.1	< 0.1	< 0.1	< 0.1	< 0.1	< 0.1	< 0.1	< 0.1
Rb	ppm	3.4	5.8	29.7	1.1	0.4	0.2	0.5	< 0.1	< 0.1	0.1	0.4	0.8	< 0.1
Sr	ppm	438.3	636.3	646.6	35.1	20.3	25.3	22.1	22.3	151.4	26	101.4	50.8	133.9
Ta	ppm	0.1	0.1	< 0.1	< 0.1	< 0.1	< 0.1	< 0.1	< 0.1	< 0.1	< 0.1	< 0.1	< 0.1	< 0.1
Th	ppm	0.7	< 0.2	< 0.2	< 0.2	< 0.2	< 0.2	< 0.2	< 0.2	< 0.2	< 0.2	< 0.2	< 0.2	< 0.2
U	ppm	0.4	0.6	< 0.1	< 0.1	0.2	0.2	0.1	0.1	0.1	0.6	0.2	0.4	< 0.1
V	ppm	45	124	48	24	63	69	72	74	62	101	77	54	40
W	ppm	< 0.5	< 0.5	< 0.5	0.7	< 0.5	< 0.5	< 0.5	< 0.5	< 0.5	< 0.5	< 0.5	< 0.5	< 0.5
Zr	ppm	99.1	2.8	3	1.5	3.1	4.5	3.4	2.6	1	2.2	1.9	2.3	0.6
Y	ppm	3.2	37.1	46.7	6.3	3.1	2.7	2.3	1	2.2	0.7	1.2	< 0.1	1.8
La	ppm	3.1	111.3	44.2	3.5	1.8	0.6	1.2	0.8	1.5	1.6	1.5	0.9	1.3
Ce	ppm	4.6	69.1	0.5	0.4	0.6	0.8	1.1	0.7	0.6	0.8	0.8	< 0.1	0.5
Pr	ppm	0.68	27.63	7.05	0.41	0.14	0.15	0.15	0.06	0.11	0.08	0.09	0.03	0.12
Nd	ppm	2.4	100	30.8	2	0.8	0.9	0.8	< 0.3	0.5	0.4	0.4	< 0.3	0.7
Sm	ppm	0.42	17.98	6.77	0.36	0.18	0.24	0.21	0.08	0.09	0.08	0.15	< 0.05	0.18
Eu	ppm	0.13	5.33	2.49	0.15	0.08	0.11	0.1	0.04	0.05	0.03	0.05	< 0.02	0.07
Gd	ppm	0.52	15.2	7.88	0.56	0.3	0.36	0.34	0.15	0.22	0.12	0.17	< 0.05	0.26
Tb	ppm	0.09	2.29	1.24	0.09	0.05	0.07	0.04	0.02	0.02	0.02	0.02	< 0.01	0.03
Dy	ppm	0.49	12.89	7.11	0.51	0.3	0.43	0.34	0.16	0.18	0.18	0.16	< 0.05	0.27
Ho	ppm	0.1	2.3	1.47	0.12	0.06	0.09	0.06	0.03	0.04	0.03	0.03	< 0.02	0.06
Er	ppm	0.31	6.19	3.93	0.3	0.2	0.3	0.23	0.11	0.11	0.09	0.12	< 0.03	0.18
Tm	ppm	0.05	0.85	0.46	0.04	0.03	0.03	0.03	0.01	0.02	0.02	0.01	< 0.01	0.01
Yb	ppm	0.35	5.35	2.53	0.22	0.17	0.25	0.19	0.1	0.05	0.1	0.08	< 0.05	0.19
Lu	ppm	0.05	0.78	0.4	0.03	0.03	0.03	0.03	0.01	< 0.01	0.02	< 0.01	< 0.01	0.02
REEs	ppm	13.29	377.19	116.83	8.69	4.74	4.36	4.82	2.27	3.49	3.57	3.58	0.93	3.89
Ce/Ce*		0.76	0.30	0.01	0.08	0.29	0.64	0.62	0.77	0.36	0.54	0.52	0.15	0.31
Eu/Eu*		0.80	0.93	0.98	0.96	0.99	1.08	1.08	1.05	1.03	0.88	0.90	1.15	0.93
UMIA		26.86	74.24	17.85	7.34	18.73	28.02	18.13	12.59	9.03	11.91	13.34	17.95	6.89

Unit abbreviations: D = duricrust; L = limonite; S = Saprolite; S-P = Serpenitized protolith.

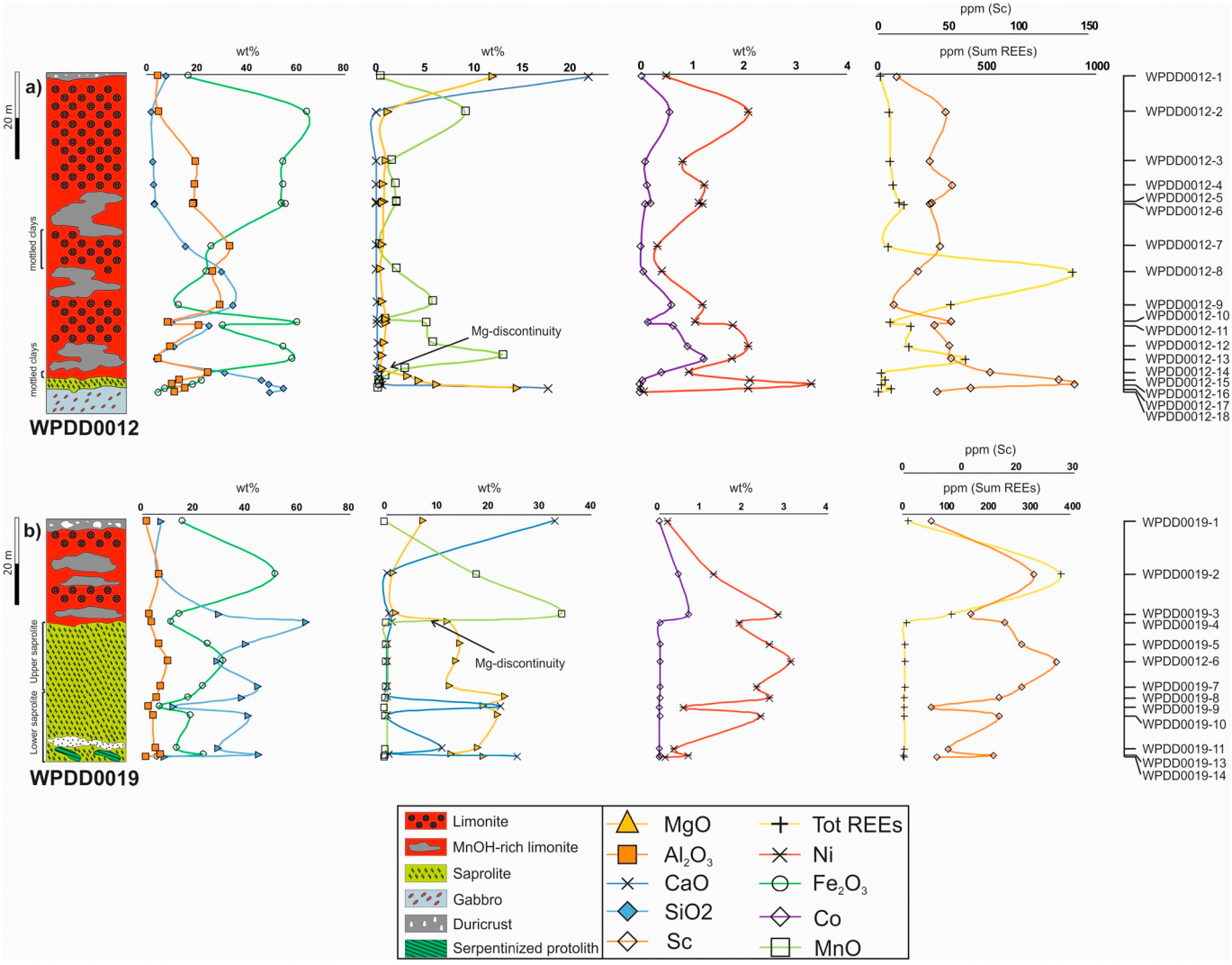

Fig. 5. Geochemical logs for drill cores WPDD0012 (a) and WPDD0019 (b): Ni, Co, Fe_2O_3, SiO_2, Al_2O_3, CaO, MgO and MnO are expressed in weigh percent (wt%); Sc and Sum REEs in parts per million (ppm).

lateritic profile, Fe_2O_3 has a behavior similar to SiO_2, except for the upper saprolite sample WPDD0019-6, where Fe_2O_3 sharply increases and SiO_2 decreases. Similar to core WPDD0012, Fe_2O_3 reaches its highest values in the limonite zone (average value: 32.23 wt%), and then decreases toward the duricrust (14.99 wt%). Al_2O_3 shows remarkable differences in its geochemical behavior and, generally, the weathering profile intercepted by the core WPDD0019 is sharply "Al_2O_3-depleted" if compared to that of the core WPDD0012. This difference can be observed starting from the locally serpentinized protolith, where Al_2O_3 has very low values (0.85 wt%). Al_2O_3 slightly increases in the saprolite (5.21 wt%) and in the limonite (4.19 wt%) zones, and decreases in the duricrust (1.18 wt%). On the whole, a similarity between the behavior of this oxide and that of Fe_2O_3 in the whole profile has been observed.

The geochemical trends of MgO and CaO are significantly different in the WPDD0019 drillcore if compared to the WPDD0012 core. The MgO content of the local parent rock is sharply higher (18.93 wt%), compared to that of the parent rock of WPDD0012. This oxide has an articulated trend: it initially experiences a decrease in correspondence of the transition zone to the lower saprolite, then undergoes a strong enrichment in the lower saprolite zone (WPDD0019-8 to WPDD0019-13), where it reaches its highest values (average value: 18.79 wt%). MgO content then decreases significantly at the transition to the upper saprolite (WPDD0019-4 to WPDD0019-7, average value: 12.95 wt%) and to the limonite zone (1.50 wt%). Finally, MgO increases to a value of 7.18 wt% in the duricrust. CaO is the dominant oxide in the local weathered parent rock, with a value of 25.36 wt%. CaO displays very low baseline values (between 0.1 and 1 wt%) throughout the lateritic profile, except for positive peak values corresponding to the saprolite samples WPDD0019-9 and WPDD0019-11 (22.07 and 10.66 wt% respectively) and to the duricrust (32.82 wt%).

MnO and Co have very similar trends to those observed in WPDD0012. The initial MnO content (0.05 wt%) of the local weathered parent rock is lower than that of the core WPDD0012, whereas its Co value is significantly higher (0.01 wt%). The MnO and Co values of the whole saprolite zone are negligible (average values: 0.24 and 0.02 wt% respectively), whereas a strong increase is observable within the limonite zone (average values: 25.69 and 0.57 wt% respectively). The concentration of both elements decreases in the duricrust, reaching values of 0.03 and 0.004 wt% respectively. Similar to Co, the Ni grade of the local parent rock (0.14 wt%) is higher than that of WPDD0012. Nickel exhibits a strong enrichment within the saprolite zone (average value: 1.83 wt%), and the distinctive features of its geochemical behavior can be commonly observed between the lower and the upper saprolite zones. In particular, the lower saprolite has a poorer Ni-enrichment (average value: 1.32 wt%) in comparison to the upper saprolite zone (2.47 wt%). In addition, the Ni trend in the lower saprolite is very similar to the SiO_2 and Fe_2O_3 trends and, with the exception of

sample WPDD0019-13, to that of MgO. In contrast, the Ni-SiO_2-Fe_2O_3 correlation cannot be observed in the upper saprolite zone, where the tendency in the highest Ni value (WPDD0019-6, 3.10 wt%) is positively correlated to that of Fe_2O_3. Ni undergoes a strong increase in the transition to the limonite (average value: 2.04 wt%), then it decreases toward the duricrust (0.20 wt%). Similarly to the core WPDD0012, Ni tendency in the limonite zone highlights the geochemical affinity of this element with Co and Mn.

4.2. High-tech metals geochemistry

4.2.1. Drillcore WPDD0012

The REEs and Sc trends throughout the laterite profile intercepted by the core WPDD0012 are shown in Fig. 5a. The dominant REEs are Ce, Nd and La with low average values of 62, 27 and 21 ppm in the whole profile. The REEs concentration in the local magmatic bedrock is significantly lower (WPDD0012-18, 6 ppm). These elements undergo a slight increase in the saprolite unit (WPDD0012-15 to WPDD0012-17, average value = 40 ppm in total). The highest total REEs values can be observed in correspondence of the Mn-(hydr)oxides-rich zones (sample WPDD0012-13, 404 ppm) and in the mottled layers within the limonite unit (samples WPDD0012-8 and WPDD0012-9, 891 and 336 ppm respectively). The REEs concentration decreases significantly in the duricrust (WPDD0012-1, 13 ppm).

The REEs/chondrite normalized patterns of core samples from the core WPDD0012 (Fig. 6a) show a progressive REEs-enrichment starting from the bedrock (WPDD0012-18, average REEs/cho value: 2 times) to the saprolite (WPDD0012-15 to WPDD0012-17, average REEs/cho value: 17 times) and then to the limonite zones (WPDD0012-2 to WPDD0012-14, average REEs/cho value: 50 times). The duricrust unit shows a sharp depletion in REEs (WPDD0012-1, average REEs/cho value: 3 times).

The majority of samples display distinctive features, such as Ce and Eu anomalies, flat HREEs patterns and steep LREEs patterns. The Ce and Eu anomalies have been quantified with the Ce/Ce*, Eu/Eu* indexes (Fig. 6b). The Ce/Ce* index varies broadly (0.04 to 8.23) and, with the exception of the limonite sample WPDD0012-7, it displays positive values in the uppermost zone of the local weathering profile (WPDD0012-1 to WPDD0012-9). In contrast, the Ce/Ce* negative values have been observed mostly in the lower limonite zone down core. The Eu/Eu* index ranges between 0.21 and 0.88. The highest Eu/Eu* values are observed in the gabbro bedrock (WPDD0012-18, 0.88), whereas variably strong negative anomalies occur throughout the local laterite profile, with the lowest values associated with the mottled clays

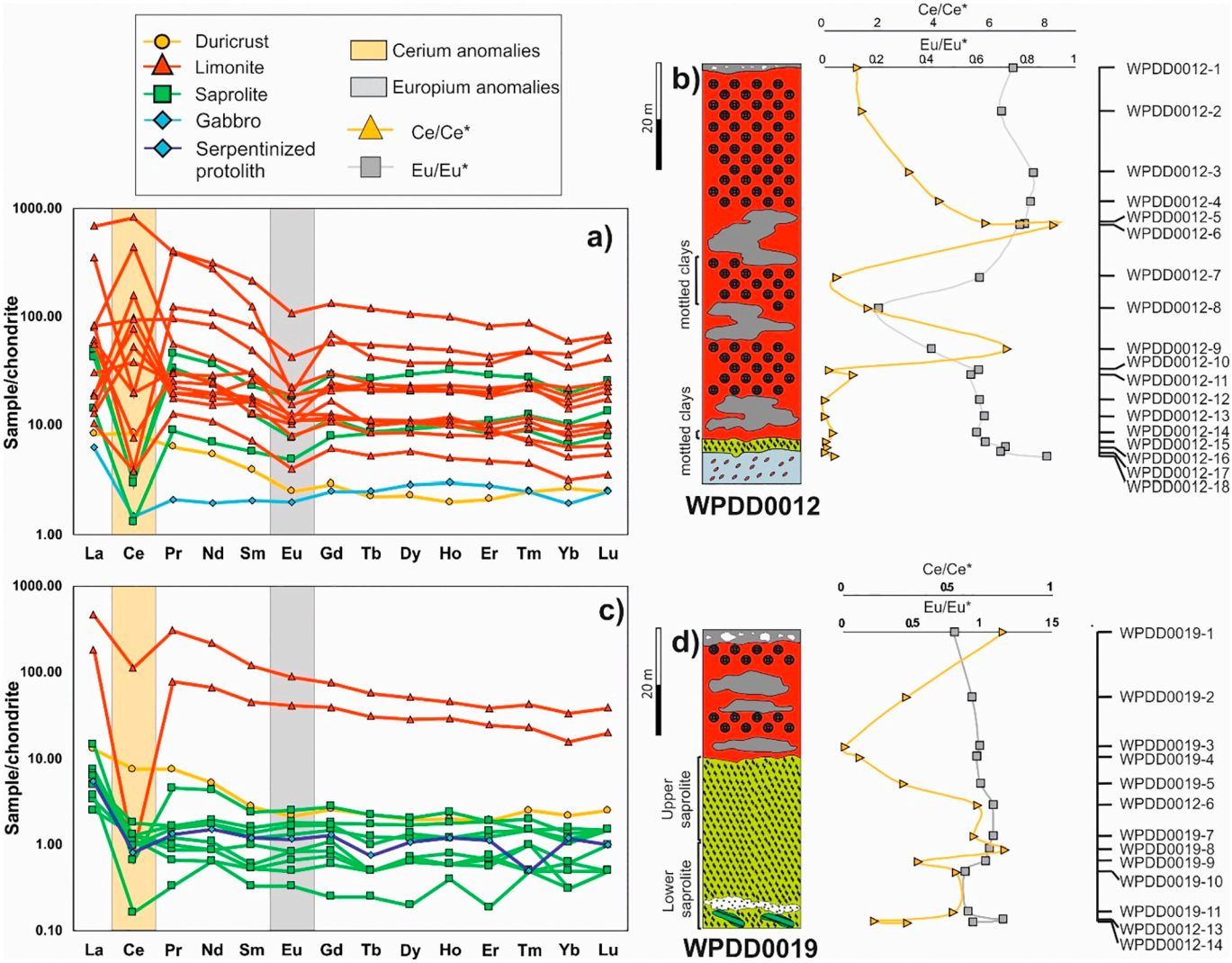

Fig. 6. a) REEs/Chondrite normalized diagrams of core WPDD0012. The chondrite reference values are taken from McDonough and Sun (1995); b) Ce/Ce* and Eu/Eu* geochemical logs of core WPDD0012; c) REEs/Chondrite normalized diagrams of core WPDD0019; d) Ce/Ce* and Eu/Eu* geochemical logs of core WPDD0019. The chondrite reference values are taken from McDonough and Sun (1995); The Ce/Ce* and Eu/Eu* anomalies have been quantified following the formulae proposed by [Eu/Eu* = [Eun / √(Smn · Gdn); Ce/Ce* = Cen / √(Lan · Prn)], (Mongelli et al., 2014)].

Table 3
Correlation matrix of drillcore WPDD0012 (data expressed as Pearson Correlation Coefficient).

	SiO_2	Al_2O_3	Fe_2O_3	MgO	CaO	MnO	Ni	Co	Sc	REE*	Ce	Eu
SiO_2	1.00	0.16	−0.85	0.42	0.11	−0.38	0.23	−0.31	0.50	−0.09	0.08	−0.29
Al_2O_3	0.16	1.00	−0.29	−0.40	−0.37	−0.28	−0.39	−0.23	−0.20	−0.01	0.49	−0.31
Fe_2O_3	−0.85	−0.29	1.00	−0.60	−0.44	0.47	0.12	0.40	−0.16	0.14	−0.16	0.40
MgO	0.42	−0.40	−0.60	1.00	0.91	−0.40	−0.23	−0.39	−0.02	−0.31	−0.27	−0.29
CaO	0.11	−0.37	−0.44	0.91	1.00	−0.28	−0.45	−0.27	−0.28	−0.23	−0.18	−0.24
MnO	−0.38	−0.28	0.47	−0.40	−0.28	1.00	0.28	0.93	−0.20	0.54	0.05	0.76
Ni	0.23	−0.39	0.12	−0.23	−0.45	0.28	1.00	0.29	0.68	−0.02	−0.29	0.22
Co	−0.31	−0.23	0.40	−0.39	−0.27	0.93	0.29	1.00	−0.17	0.50	−0.04	0.78
Sc	0.50	−0.20	−0.16	−0.02	−0.28	−0.20	0.68	−0.17	1.00	−0.18	−0.39	−0.08
REE*	−0.09	−0.01	0.14	−0.31	−0.23	0.54	−0.02	0.50	−0.18	1.00	0.56	0.75
Ce	0.08	0.49	−0.16	−0.27	−0.18	0.05	−0.29	−0.04	−0.39	0.56	1.00	−0.03
Eu	−0.29	−0.31	0.40	−0.29	−0.24	0.76	0.22	0.78	−0.08	0.75	−0.03	1.00

REE* = total Rare Earth Elements expect for Ce and Eu.

horizon between samples WPDD0012-8 and WPDD0012-9 (0.21 and 0.42 respectively).

As shown in Fig. 5a, Sc sharply increases at the boundary between the gabbro (sample WPDD0012-18, 42 ppm) and the saprolite zone (samples WPDD0012-17 to WPDD0012-15). In the latter zone, scandium reaches the highest values of the core (average of 111 ppm). Toward the upper part of the profile, this element has a constant negative trend, reaching very low values (average value: 50 ppm). In addition, the Sc trend does not show any type of correlation to Fe_2O_3 wt% (Fig. 5a), whereas a similarity between the Ni and the Sc trends has been observed throughout the profile (Fig. 5a).

To better constrain the High-Tech (HT) metals geochemical deportment, and to infer about their possible mineralogical association, a correlation matrix between the HT metals and the most representative major oxides as well as Ni and Co has been calculated (Table 3). It must be specified that during this analysis Ce, Eu and the other REE (i.e. REE*) have been processed separately. In general, the correlation matrix confirms that the REE* are chiefly associated with both MnO (r = 0.54, p-value = 0.02) and Co (r = 0.50, p-value = 0.04). As expected, Ce and Eu behave differently from the other REEs. Firstly, although the Ce-REE* (r = 0.56, p-value = 0.01) and Eu-REE* (r = 0.75, p-value = 0.00) correlations are positively high, they are quite lower than the unity. In addition, differently from the other REEs*, Ce is not correlated to MnO (r = 0.05, p-value = 0.86). However, the most striking feature of the Ce behavior is its positive correlation with Al_2O_3 (r = 0.49, p-value = 0.04). Eu displays a sharp positive correlation with REE* (r = 0.75, p-value = 0.00), and similar to other REE*, it is correlated with Co (r = 0.78, p-value = 0.00) and MnO (r = 0.76, p-value = 0.00). Finally, Sc shows remarkable positive correlations with Ni (r = 0.68, p-value = 0.00) and SiO_2 (r = 0.50, p-value = 0.03), whereas it does not show any correlations with Fe_2O_3 (r = −0.16, p-value = 0.54).

4.2.2. Drillcore WPDD0019

Fig. 5b shows the REEs and Sc geochemical trends in WPDD0019. Also in this core La, Nd, and Ce are the main REEs with average values of 13, 10 and 6 ppm. In this core, even though the local parent rock displays a similar total REEs concentration (WPDD0019-14, 5 ppm) to that of the WPDD0012 core, the lateritic profile shows a general REEs-depletion. In particular, the total REEs concentration remains very low in the whole saprolite unit (WPDD0019-4 to WPDD0019-13, average value: 4 ppm), whereas a significant increase is observed in the limonite zone (WPDD0019-2 to WPDD0019-3, average value: 247 ppm). REEs sharply decrease in the duricust (WPDD0019-1, 13 ppm). In this core the strong REEs enrichment within the limonite zone is positively correlated with a Fe_2O_3 (Fig. 5b).

As shown by the REEs/cho diagram in Fig. 6c, the highest REEs/cho values occur in the limonite zone (WPDD0019-2 to WPDD0019-3, average REE/cho: 83 times), whereas very low REEs/cho enrichments characterize the serpentinized parent rock (WPDD0019-14, average REEs/cho: 1.4 times), the saprolite zone (WPDD0019-4 to WPDD0019-13, average REEs/cho: 1.5 times) and the duricrust (WPDD0019-1, average REEs/cho: 4 times).

Cerium and Eu display several differences in their geochemical behaviors in this core. In particular, Ce always shows negative anomalies throughout the local weathering profile. In addition, the Ce/Ce* index has a very irregular trend (Fig. 6d), and a narrow range of values (0.01–0.77). Another remarkable difference in the geochemical behavior of REEs in this core respect to the previous core, regards Eu. The initial Eu/Eu* ratio of the serpentinized parent rock in this core (WPDD0019-14, 0.93) is higher than in the core WPDD0012. In addition, differently from the latter drillcore, Eu does not yield anomalies (Fig. 6c) and, as shown by Fig. 6d, the Eu/Eu* ratio is relatively more constant, with values ranging between 0.80 and 1.15.

Fig. 5b shows the scandium trend in the core WPDD0019. Even though in this core Sc has very low concentrations (5–27 ppm), its geochemical trend is significantly different to that measured in the core WPDD0012. In particular, the geochemical behavior of Sc in WPDD0019 is very similar to the behavior of Fe_2O_3 and Ni (Fig. 5b). Nevertheless, the highest Sc concentrations are detected in the limonite sample WPDD0019-2 and in the saprolite sample WPDD0019-6 (23 and 27 ppm respectively).

The correlation matrix of the core WPDD0019 (Table 4) confirms that the High-Tech metals deportment in this core is different from WPDD0012. In particular, although the REE*-Co (r = 0.76, p-value = 0.00) and the REE*-MnO (r = 0.70, p-value = 0.01) correlations are high, a strong REE* correlation has been observed also with Fe_2O_3 (r = 0.71, p-value = 0.01). Furthermore, the REE*-Ce (r = 0.93, p-value = 0.00) and REE*-Eu (r = 1.00, p-value = 0.00) associations are remarkably higher, if compared to those of the previous core. As a corollary, Eu and REE*, and less Ce, display variably similar positive correlations with Fe_2O_3 (r = 0.68, p-value = 0.01; r = 0.71, p-value = 0.01; r = 0.79; p-value = 0.00, respectively), MnO (r = 0.75, p-value = 0.00; r = 0.70, p-value = 0.01; r = 0.39, p-value = 0.19, respectively) and Co (r = 0.82, p-value = 0.00; r = 0.76, p-value = 0.00; r = 0.48, p-value = 0.10, respectively). Finally, the strong Ce-Al_2O_3 positive correlation observed in the WPDD0012 core is not present in the WPDD0019 profile (r = 0.18, p-value = 0.55). Regarding Sc, although also in this drillcore positive correlations have been observed with SiO_2 and Ni (r = 0.46, p-value = 0.11; r = 0.75, p-value = 0.00 respectively), the correlation matrix confirms its strongly different deportment. In fact, remarkable positive correlations have been detected also with Al_2O_3 and Fe_2O_3 (r = 0.85, p-value = 0.00; r = 0.74, p-value = 0.00, respectively).

4.3. The ultramafic index of alteration (UMIA)

In order to assess the geochemical variations triggered by the

Table 4
Correlation matrix for drillcore WPDD0019 (data expressed as Pearson Correlation Coefficient).

	SiO_2	Al_2O_3	Fe_2O_3	MgO	CaO	MnO	Ni	Co	Sc	REE	Ce	Eu
SiO_2	1.00	0.34	−0.11	0.21	−0.68	−0.20	0.52	−0.21	0.46	−0.40	−0.43	−0.39
Al_2O_3	0.34	1.00	0.70	−0.03	−0.70	−0.13	0.52	−0.07	0.85	0.10	0.18	0.08
Fe_2O_3	−0.11	0.70	1.00	−0.49	−0.51	0.25	0.30	0.34	0.74	0.71	0.79	0.68
MgO	0.21	−0.03	−0.49	1.00	0.10	−0.72	−0.04	−0.75	−0.17	−0.71	−0.55	−0.73
CaO	−0.68	−0.70	−0.51	0.10	1.00	−0.25	−0.77	−0.29	−0.83	−0.23	−0.14	−0.24
MnO	−0.20	−0.13	0.25	−0.72	−0.25	1.00	0.26	0.99	0.05	0.70	0.39	0.75
Ni	0.52	0.52	0.30	−0.04	−0.77	0.26	1.00	0.27	0.75	0.03	−0.11	0.06
Co	−0.21	−0.07	0.34	−0.75	−0.29	0.99	0.27	1.00	0.11	0.76	0.48	0.82
Sc	0.46	0.85	0.74	−0.17	−0.83	0.05	0.75	0.11	1.00	0.27	0.31	0.26
REE*	−0.40	0.10	0.71	−0.71	−0.23	0.70	0.03	0.76	0.27	1.00	0.93	1.00
Ce	−0.43	0.18	0.79	−0.55	−0.14	0.39	−0.11	0.48	0.31	0.93	1.00	0.90
Eu	−0.39	0.08	0.68	−0.73	−0.24	0.75	0.06	0.82	0.26	1.00	0.90	1.00

REE* = total Rare Earth Elements expect for Ce and Eu.

chemical weathering, the ultramafic index of alteration (UMIA) has been calculated in the considered profiles. This calculation has been performed following the formula proposed by Babechuk et al. (2014) and by Aiglsperger et al. (2016):

$$UMIA = 100 \times [(Al_2O_3 + Fe_2O_{3(t)})/(Al_2O_3 + Fe_2O_3 + SiO_2 + MgO)]$$

In the MgO-SiO_2-(Al_2O_3 + $Fe_2O_{3(t)}$) ternary plot (Fig. 7) the geochemical trend of the profile intercepted by core WPDD0012 is characterized by an initial loss of MgO in the transition between the gabbro (WPDD0012-18, UMIA: 13.45) and the saprolite zone (WPDD0012-15 to WPDD0012-17, average UMIA value: 22.55). Afterwards, a strong SiO_2 depletion has been observed in the limonite zone, where the UMIA index reaches its highest values (UMIA range values in limonite: 47.24–89.68), with the exception of relatively low UMIA values detected in the mottled clays-rich horizons (e.g. WPDD0012-8 to WPDD0012-9, average UMIA value: 46.61). The duricrust (WPDD0012-1) lies outside the "classic" lateritization trend, because it shows a lower UMIA (27.22) and a relative gain in both MgO and SiO_2.

In the core WPDD0019, the serpentinized protolith (WPDD0019-14) has a low UMIA value (6.89) and, if compared to the gabbro of the core WPDD0012, it has a higher MgO content. Also in this case the saprolite unit shows a progressive loss in MgO and, if compared to the losses occurring in the WPDD0012 drillcore, it results in a lower UMIA average value (about 15). In general, the thin limonite zone of the core WPDD0019 shows a lower UMIA (WPDD0019-2 to WPDD0019-3, average UMIA value: 46.05), if compared to the values calculated in the previous core. In particular, the bottom specimen of the limonite zone (WPDD0019-3) falls within the saprolite field, whereas the limonite sample WPDD0019-2 has a similar UMIA value (74.24) to that calculated in limonite core samples from the core WPDD0012. Also in this core, the duricrust (WPDD0019-1) is located outside the general trend, with an UMIA value of 26.86.

5. Discussion

5.1. Ni- and Co-grades and geochemical evolution of the studied profiles

The results of the whole-rock chemical analysis have shown the geochemical complexity of the Wingellina orebody. The laterite profiles intercepted by the two studied drillcores show similar Ni-grades (WPDD0012: 1.42 wt% Ni; WPDD0019: 1.73 wt% Ni). The results obtained indicate that, even though the Wingellina laterite is an oxide-type deposit, the silicate zones (i.e. saprolite horizon) also display remarkably high Ni-grades (WPDD0012, average Ni-grade: 2.52 wt%; WPDD0019, average Ni-grade: 1.83 wt%). Therefore, as proposed by many authors (e.g. Berger et al., 2011; Tauler et al., 2017), the classification of the Ni-laterites based on the dominant ore-bearing mineralogy (i.e. oxide-type, clay silicate-type and hydrous Mg silicate-type, e.g. Freyssinet et al., 2005; Golightly, 2010) is an oversimplification, which must be applied with care. Cobalt displays high values in the core WPDD0012 (0.28 wt% Co), whereas it is less enriched in the core WPDD0019 (0.09 wt% Co); in general the highest Co concentrations are found within the limonite zones (WPDD0012, average Co-grade: 0.39 wt%; WPDD0019 average Co-grade: 0.57 wt%).

The geochemical evolution of the Wingellina laterite profiles, together with the drillcore characteristics, have provided useful insights about the influence of a range of external controlling factors (e.g. bedrock lithology, drainage conditions, climate etc.) on the local ore-forming processes. The two mineralized laterite profiles of WPDD0012 and WPDD0019 drillcores have both similar, as well as different features.

As shown by the geochemical logs (Fig. 5a, b), exemplified in the MgO-SiO_2-(Al_2O_3 + Fe_2O_3) ternary plot (Fig. 7), the transition zones between the parent rocks and the saprolite units of the two laterite profiles are both characterized by a sharp drop in the MgO concentration and by a gain of SiO_2 and Ni. Nevertheless, the genesis of the silicate-rich unit of the core WPDD0012 is marked by a significantly higher Al_2O_3 gain (Al_2O_3 average values in the saprolite: 13.32 wt%), if compared with that of the core WPDD0019 (Al_2O_3 average values in the lower saprolite: 4.34 wt%). This remarkable geochemical difference between the two laterite profiles suggests the occurrence of different saprolitization processes, which are likely related to the variable bedrock mineralogy and geochemistry. Regarding the WPDD0012 profile, the above mentioned geochemical evolution suggests that the hydrolysis of the primary minerals of the local parent rock (clinopyroxenes, orthopyroxenes, plagioclase and subordinate forsterite) has enhanced the formation of a smectite-rich saprolite horizon (Putzolu, 2017). This characteristic is consistent with the observations of other authors (Nahon et al., 1982; Colin et al., 1990), who discovered that under intense weathering conditions the incongruent dissolution of pyroxenes is the main trigger for the neo-formation of Ni-bearing smectites. In addition, the Al_2O_3 gain in the saprolite zone is consistent with the direct precipitation (neo-formation) of smectite (e.g. montmorillonite) from pyroxenes (Freyssinet et al., 2005).

In the silicate-dominant laterite of the WPDD0019 profile, the unweathered bedrock is not intersected by the drillhole. However, the geochemical characteristics of the deeply serpentinized protolith (i.e. saprock), occurring within the local saprolite, suggest a potential variation of the parent rock lithology. In particular, the Eu/Eu* ratio observed in the WPDD0019 saprock is slightly higher (Eu/Eu* = 0.93) than that of the fresh parent rock intercepted by the core WPDD0012 (WPDD0012-18, Eu/Eu* = 0.88). This geochemical difference would suggest that the WPDD0019 laterite profile is developed from a more primitive lithology, likely corresponding to one of several peridotite units occurring in the Wingellina Hill mafic to ultramafic layered intrusion (Ballhaus and Glikson, 1989). The primary components of the Wingellina Hill magmatic sequence correspond mainly to websterite and wehrlite (Ballhaus and Glikson, 1989). Therefore, the geochemical

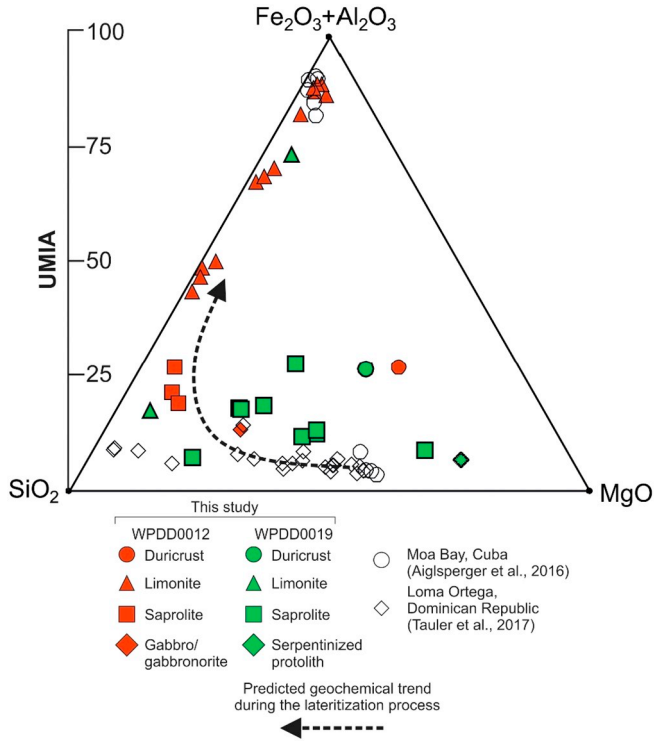

Fig. 7. MgO-SiO_2-(Al_2O_3 + Fe_2O_3) molar ternary plot, showing the geochemical variations during the chemical weathering of cores WPDD0012 and WPDD0019 and the comparison to those of the mineralized laterites of Moa Bay, Cuba (Aiglsperger et al., 2016) and Loma Ortega, Dominican Republic (Tauler et al., 2017).

and mineralogical characteristics (Putzolu, 2017) observed in the lower saprolite in the drillcore from this locality suggest a strong control of the parent rock mineralogy (mostly ferromagnesian minerals) on the ore-forming process, which was probably dominated by hydrothermal alteration and serpentinization, rather than by neoformation of clays after weathering (as in the case of drillcore WPDD0012). This fact is in agreement with previous literature data, which consider the serpentinization process to be commonly affecting the olivine- and pyroxene-rich protoliths, i.e. prevailingly ultramafic rocks (McCollom and Seewald, 2013).

Another characteristic of the saprolite horizon in the core WPDD0019 is the "zoned" geochemical trend of MgO. More in detail, the MgO amount strongly increases in the lower saprolite, whereas it decreases within the upper saprolite. The progressive MgO loss is coeval with a significant increase in concentration of Fe_2O_3 and locally even with a high Ni-grade. This particular feature suggests an instability increase in the serpentines occurring in the lower saprolite, and hence the neo-formation of secondary serpentines, and of clay minerals and Fe-hydroxides (Golightly and Arancibia, 1979; Freyssinet et al., 2005), according to the following reactions:

$$Mg_3Si_2O_5(OH)_4 + Ni^{2+} = (Mg,Ni)_3Si_2O_5(OH)_4 + Mg^{2+} \quad (1)$$

primary serpentine — Ni-serpentine

$$2(Mg,Fe)_3Si_2O_5(OH)_4 + 3H_2O = Mg_3Si_4O_{10}(OH)_2{*}4H_2O + 2Mg^{2+} + FeOOH + 3OH^- \quad (2)$$

primary serpentine — smectite — goethite

$$(Mg,Fe)_3Si_2O_5(OH)_4 + 3H^+ = FeOOH + 2SiO_2 + 2Mg^{2+} + 3H_2O \quad (3)$$

primary serpentine — goethite — quartz

The occurrence of secondary silica veins and boxworks within the local upper saprolite zone (Fig. 4e) is consistent with the observations carried out by other authors on other deposits (e.g. Golightly, 1981; Tauler et al., 2017), who affirmed that in poorly drained systems the weathering of serpentines enhances the formation of quartz and clay minerals. In the specific case of the profile intersected by the core WPDD0019, the occurrence of a thick, massive and poorly jointed serpentinite could have prevented the complete leaching of silica, thus explaining also the poor development of the local limonitic orebody and the generally low UMIA values (Fig. 7).

Several analogies in the geochemistry of the limonite zones in the two studied profiles have been detected. Firstly, the transition toward the limonite zone in both profiles is marked by the complete leaching of MgO (the "Mg-discontinuity"; Brand et al., 1998), SiO_2 and Al_2O_3 and by a significant gain of Fe_2O_3 (Figs. 5a, b and 7). These geochemical trends could reflect the progressive acidification of the soil solutions, commonly occurring in the uppermost zone of the weathering profile (Golightly, 2010), thus enhancing the instability of the silicate phases (i.e. smectitic clay and/or serpentine) and the precipitation of late-stage Fe-(hydr)oxides (Nahon et al., 1982). In this framework, it is known that the vertical variation in pH strongly affects the paragenetic evolution of the mineralogical association within the laterite profiles, thus controlling the Ni deportment and its speciation (Golightly, 1981, 2010). This process is well displayed by the Ni geochemistry in both the studied profiles. In particular, the Ni distribution (Fig. 5a and b) is positively correlated with SiO_2 in the saprolite, whereas within the limonite zone it is correlated with MnO, Co and to a less extent to Fe_2O_3, thus confirming that the highest-grade zones of the limonitic orebody are characterized mainly by the occurrence of Mn-(hydr)oxides (Putzolu et al., 2018). In this context, Co is found to be strictly associated with MnO throughout the laterite profiles of both drillcores, with the highest grade observed within the limonite units. This geochemical affinity has been described by many authors (e.g. McKenzie, 1989), who argued about the capability of the Mn-(hydr)oxides to uptake Co due to their fine particle sizes, which offer a large surface area for metal adsorption. During lateritization also the Mn distribution, and thus the precipitation of Co(Ni)-bearing Mn-(hydr)oxides, is controlled by the Eh-pH variation in the weathering profile. In both the studied profiles, the first significant gain of MnO occurs in the lowermost part of the limonite zones, at the transition with the saprolite sections. This MnO behavior is quite common in Ni-Co laterite. In fact, as shown by Dublet et al. (2017), the early stage weathering (i.e. saprolitization) of the parent rock promotes the oxidation of Mn^{2+} to Mn^{3+} and lastly to the most stable ionic species, Mn^{4+}. This process stimulates an efficient precipitation of Mn-(hydr)oxides at the transition from the saprolite toward the limonite zone, along which higher humidity and a slightly more alkaline pH enhance the stabilization of such phases (Dublet et al., 2017).

The main geochemical difference between the two limonite units is that the limonite orebody of the core WPDD0012 is locally characterized by the occurrence of few Al_2O_3-rich and Fe_2O_3-poor zones, which are mirrored by the kaolinite-rich mottled clay horizons. This difference can be mainly ascribed to the higher input of Al_2O_3 provided by the local gabbro/gabbronorite bedrock, which resulted in the neo-formation of kaolinite-rich zones within the limonitic body.

A significant enrichment of the mobile elements (i.e. Mg, Ca and Si) and a decrease in Fe, Al, and Mn (together with the Ni- and Co-grades) occurs at the boundary between the limonite and the duricrust in both drillcores (Figs. 5a, b and 7). These geochemical trends can provide interesting information about the post-formation process that affected the geochemical evolution of the Wingellina orebody, because they can reflect a significant climatic variation, leading to a decrease of the weathering rate and to calcification and silicification processes in the uppermost zone of the laterite profile (Golightly, 2010). In the Australian Ni-Co laterite deposits of the Yilgarn craton, this post-formation process was caused by the northeasterly drifting of the continent starting in Tertiary (mid-Miocene), which consequently produced an increased aridity during Late Miocene-Pliocene. Thus, both calcification and silicification processes prevailed over ferruginization in the

uppermost sections of the laterite profiles (Tardy and Roquin, 1998; Anand and Paine, 2002).

5.2. Geochemical behavior of REEs and Sc

5.2.1. Rare Earth Elements

The geochemical behavior of REEs is very variable in the Wingellina laterite. In the analyzed samples, these elements are preferentially concentrated within the limonite zones of the studied profiles, where their concentration reaches values up to 890 ppm. The REEs speciation is strongly controlled by the mineralogical characteristics of the limonitic ore. In particular, a positive correlation of the REEs with MnO (Tables 3 and 4) could suggest that the remobilization of lanthanides and their accumulation in Mn-(hydr)oxides was due to chemical weathering, which is commonly enhanced by bacterial activity (Davranche et al., 2005; Laskou and Economou-Eliopoulos, 2007; Pourret et al., 2010; Vodyanitskii, 2012; Kalatha and Economou-Eliopoulos, 2015; Aiglsperger et al., 2016). In addition, the correlation of REEs with the most representative oxides, as well as with Ni and Co in the core WPDD0012 (Table 3) shows that a significant geochemical and mineralogical decoupling occurred between Ce, Eu and the other REE (i.e. REE*). In particular, REE* and Eu are chiefly associated with MnO and Co. As reported by Putzolu et al. (2018), the MnO- and Co-rich horizons of the Wingellina limonitic orebody contain lithiophorite-asbolane intermediates, which, as reported by Mongelli et al. (2015), can scavenge REEs through sorption processes in supergene settings.

Cerium has a very different behavior, which is highlighted both by the positive correlation with Al_2O_3 (Table 3), and by the REEs chondrite normalized patterns (Fig. 6a and c), where several Ce positive and negative anomalies can be observed. In general, these anomalies produced under a weathering regime, are mainly due to the oxidation of cerium from trivalent (Ce^{3+}) to tetravalent state (Ce^{4+}). This process could also trigger the precipitation of supergene REEs-bearing minerals such as fluoro-carbonates, Ce-oxides and phosphates (Braun et al., 1990), as already observed in other Ni-Co laterite deposits (e.g. Moa Bay in Cuba and Falcondo in the Dominican Republic, Aiglsperger et al., 2016). The higher Ce-Al_2O_3 positive correlation occurs in the WPDD0012 drillcore. The local laterite profile also shows that the highest Ce/Ce* values occur in the uppermost zone of the limonite unit, whereas the negative values occur in the lower limonite zone. This characteristic is consistent with a REEs redistribution within the orebody, and with Ce fractionation and concentration in the uppermost zone of the deposit (Mongelli et al., 2014).

Another interesting feature of the REEs geochemistry of the WPDD0012 samples is the significant REE concentration (highest REEs-amount 891 ppm) observed in the relatively MnO-poor (2.04 wt% MnO) and Al_2O_3-rich mottled zone (sample WPDD0012-8). As reported by Putzolu et al. (2018), the mottled zone of the limonitic orebody mainly consists of kaolinite, with only minor lithiophorite. The above quoted sample lies outside the MnO-REEs correlation trend (Fig. 5a), thus suggesting a different mode of REEs enrichment. Similar significant REEs-enrichments in the MnO-poor zones of the lateritic profile have been observed by Aiglsperger et al. (2016) in the mottled zones of the limonitic orebody of the Moa Bay laterite deposit (Cuba), and have been considered to be related to REE adsorption into clays, following a ion adsorption-type concentration process. However, in our case, the mottled clay sample (WPDD0012-8) is also characterized by a significant P_2O_5 concentration (0.15 wt% P_2O_5), which together with positive correlation of Ce with Al_2O_3, could also suggest the occurrence of REEs into LREE-Al-bearing phosphates. Nevertheless, both the occurrence modes need to be verified through dedicated mineralogical investigations.

The REEs patterns of the core WPDD0012 display negative Eu anomalies. As reported in the existing literature (McLennan et al., 1993) Eu should have a refractory behavior during weathering, therefore the Eu/Eu* ratio of the many horizons of the laterite profile should reflect that of the local parent rock. In the Wingellina case, the Eu/Eu* index not only varies broadly (0.21–0.83) through the laterite profile, but it is also quite different from that measured in the gabbro/gabbronorite bedrock (0.88). This anomalous behavior of Eu could be related to the original deportment of REE in the different minerals of the gabbro/gabbronorite protolith. As shown by Weill and Drake (1973), the Eu enrichment or depletion in igneous rocks is mainly due to the Eu tendency to be incorporated into plagioclases, preferentially over other minerals. Therefore, in the Wingellina case, Eu could have been mostly hosted in the plagioclases of the parent rock, whereas the other REEs were mainly hosted by accessory minerals, such as sphene, zircon and apatite (Frey et al., 1968). Therefore, the Eu/Eu* variation could be attributed to the different response to chemical weathering of REE-bearing accessory phases compared to plagioclase, which likely produced a preferential leaching of Eu in the supergene environment from the highly unstable plagioclases of the protolith, whereas the other REEs remained in the more stable REEs-bearing accessory minerals. This is in agreement with previous literature (Babechuk et al., 2014), which argued about the contribution of the occurrence of plagioclase-bearing parent rocks on the loss of Eu in the weathering products. The REEs geochemical deportment in the profile WPDD0019 is characterized by several differences, if compared to that of the WPDD0012 drillcore. Firstly, the REEs enrichment in the WPDD0019 limonite zone (up to 377 ppm) is much lower if compared to the former drillcore. The lower gain of REEs observed within core WPDD0019, together with the higher Eu/Eu* ratio, is in agreement with the development of the local laterite profile from a predominantly ultramafic protolith, depleted of incompatible elements (such as REEs). In addition, according to the correlation parameters (Table 4) and to the relatively flat REEs patterns (Fig. 6c) observed in WPDD0019, the REE*-Eu-Ce fractionation is lower if compared to that of the core WPDD0012. Therefore, one the main controlling factor of the lower REEs enrichment in the WPDD0019 laterite profile could be the less significant LREE-HREE fractionation, which prevented the neo-formation of LREE-bearing phases (Braun et al., 1990; Mongelli, 1997; Mameli et al., 2007; Mondillo et al., 2011), leading to REEs uptaking mainly in the Fe-oxyhydroxides and less in the Mn-hydroxides.

Another important variation of the REEs deportment, and more specifically of that of Ce, is their correlation with Fe_2O_3 (Fig. 5b and Table 4) that confirms the observation of other authors (e.g. Vodyanitskii, 2012), who suggested that lanthanides behave not only as manganophilic but also as siderophilic elements. Other important characteristics of the REEs geochemistry in core WPDD0019 are the absence of Eu anomalies (Fig. 6d) and the almost constant Eu/Eu* ratio (0.80–1.15, Fig. 6c), which support the absence of plagioclase from the local protolith and, differently from core WPDD0012, a homogenous leaching of REEs from the primary minerals of the protolith.

5.2.2. Scandium

The Sc content of the studied profiles of the Wingellina Ni-Co laterite deposit is significantly lower (WPDD0012, average Sc content: 54 ppm; WPDD0019, average Sc content: 15 ppm) if compared to economic deposits, where this element reaches concentration values up to 800 ppm (e.g. Syerston–Flemington, New South Wales, Australia; Chassé et al., 2016). However, the current study can provide useful information about its geochemical deportment. Firstly, the highest Sc concentrations are found within the silicate-rich zones of the sets of core samples from both WPDD0012 and WPDD0019 (maximum Sc values of 140 and 27 ppm respectively). This characteristic is in contrast with the observations carried out by Audet (2008) and Aiglsperger et al. (2016), who observed a clear tendency of Sc to concentrate in the uppermost horizons of the laterite profiles (i.e. limonite units). Secondly, the sharp difference of the Sc-grades in the two profiles considered could be interpreted in terms of a variation of the enrichment modality, and hence of the nature of Sc-bearing minerals. In fact, the Sc trend in core WPDD0019 is positively correlated with that of Fe_2O_3

(Fig. 5b and Table 4), this suggesting the uptaking of Sc^{3+} into neo-formed Fe-oxy-hydroxides (Chassé et al., 2016), which occur as sub-ordinate minerals in the saprolite unit (Putzolu, 2017). Regarding to the core WPDD0012, the Sc-Fe_2O_3 geochemical affinity was not detected and Sc is chiefly associated with and Si and Ni. This association can be interpreted as a proxy of the Sc remobilization during the lateritization process. However, the positive correlations of Sc with SiO_2 (cores WPDD0012 and WPDD0019) and with Al_2O_3 (core WPDD0019) are quite atypical. The Sc-Si association in the phyllosilicate-rich saprolite sections could potentially reflect the Sc occurrence in clay minerals. In fact, as reported by Birgu (1981), in the Fe^{3+}-bearing layered silicates (such as montmorillonite and chlorite), Sc could be able to enter in the crystal lattice as substituting for Fe^{3+} in the (di)octahedral site. However, further and more detailed mineralogical investigations are needed to better constrain the mineral deportment of this element in the Wingellina deposit.

6. Conclusions

The study of the Wingellina Ni-Co laterite deposit (Western Australia) has shown that the combination of geochemical and mineralogical data, together with a targeted analysis of the facies variability can provide an useful tool to define the controlling factors affecting the Ni and Co supergene enrichment and the main ore-forming processes acting during lateritization. The geochemical evolution of the deposit, the Ni-Co enrichment and the development of several different facies in the laterite profile are strongly affected by the heterogeneity of the parent rock lithology, which likely controlled the degree of hydrothermal serpentinization, the efficiency of the drainage system and thus the dynamics of the lateritization process.

The High-Tech metals have a variable geochemical deportment at Wingellina:

(i) REEs are remarkably concentrated within specific zones of the limonite units, which primarily correspond to Mn- and Fe-(hydr) oxides rich horizons and locally to mottled clayey Al-rich units. A significant geochemical decoupling of REEs has been also observed. The Ce deportment suggests that its speciation was locally controlled by its oxidation from Ce^{3+} to Ce^{4+} and potentially by its uptaking in Fe-(hydr)oxides at the top of the laterite profile. The other REEs are enriched within the MnO- and Fe_2O_3-rich zones of the orebody, which suggests their capture in Mn- and Fe-(hydr) oxides.

(ii) Even though the Sc enrichment in the studied laterite profiles is negligible, several geochemical proxies suggesting its remobilization and enrichment during the weathering process have been identified. The Sc geochemical behavior is variable and complex, with the higher Sc-grades observed in the silicate zones of the deposit. This feature is in contrast with previous studies carried out on other Ni-Co laterite deposits and, therefore, more detailed mineralogical assessments will be necessary to better constrain the mineralogical deportment of REEs and Sc within the Wingellina orebody.

Acknowledgments

This study is part of the ongoing PhD project of F. Putzolu at the University of Napoli “Federico II” (Italy). The authors acknowledge Metals X Limited for the technical assistance during the field and sampling activity and R. de'Gennaro for SEM analysis. This study has been partly funded by a research grant provided to F. Putzolu by the International Exchanges Program of the University of Napoli “Federico II”, and by “Programma per il finanziamento della ricerca di Ateneo 2016 -Progetto CEB”, granted by Università degli Studi di Napoli Federico II (Italy) to Dr. Nicola Mondillo. Comments and suggestions from three anonymous reviewers have greatly improved the quality of the paper.

References

Aiglsperger, T., Proenza, J.A., Zaccarini, F., Lewis, J.F., Garuti, G., Labrador, M., Longo, F., 2015. Platinum group minerals (PGM) in the Falcondo Ni-laterite deposit, Loma Caribe peridotite (Dominican Republic). Mineral. Deposita 50 (1), 105–123.
Aiglsperger, T., Proenza, J.A., Lewis, J.F., Labrador, M., Svojtka, M., Rojas-Puron, A., Longo, F., Ďurišová, J., 2016. Critical metals (REE, Sc, PGE) in Ni laterites from Cuba and the Dominican Republic. Ore Geol. Rev. 73, 127–147.
Anand, R.R., Paine, M., 2002. Regolith geology of the Yilgarn Craton, Western Australia: implications for exploration. Aust. J. Earth Sci. 49 (1), 3–162.
Audet, M.A., 2008. Le massif du Koniambo-Nouvelle Calédonie: formation et obduction d'un complexe ophiolitique de type SSZ. In: Enrichissement en nickel, cobalt et scandium dans les profils résiduels. Université de Nouvelle Calédonie (Doctoral dissertation). (327 pp.).
Babechuk, M.G., Widdowson, M., Kamber, B.S., 2014. Quantifying chemical weathering intensity and trace element release from two contrasting basalt profiles, Deccan Traps, India. Chem. Geol. 363, 56–75.
Ballhaus, C.G., Glikson, A.Y., 1989. Magma mixing and intraplutonic quenching in the Wingellina Hills Intrusion, Giles Complex, central Australia. J. Petrol. 30 (6), 1443–1469.
Berger, V.I., Singer, D.A., Bliss, J.D., Moring, B.C., 2011. Ni-Co Laterite Deposits of the World: Database and Grade and Tonnage Models. US Department of the Interior, Geological Survey, pp. 30.
Birgu, O., 1981. Scandium-iron correlation in clay minerals. Earth Planet. Sci. Lett. 55 (3), 450–452.
Brand, N.W., Butt, C.R.M., Elias, M., 1998. Nickel laterites: classification and features. AGSO J. Aust. Geol. Geophys. 17 (4), 81–88.
Braun, J.J., Pagel, M., Muller, J.P., Bilong, P., Michard, A., Guillet, B., 1990. Cerium anomalies in lateritic profiles. Geochim. Cosmochim. Acta 54 (3), 781–795.
Butt, C.R.M., Cluzel, D., 2013. Nickel laterite ore deposits: weathered serpentinites. Elements 9, 123–128.
Camacho, A., Fanning, C.M., 1995. Some isotopic constraints on the evolution of the granulite and upper amphibolite facies terranes in the eastern Musgrave Block, central Australia. Precambrian Res. 71 (1–4), 155–181.
Camacho, A., McDougall, I., 2000. Intracratonic, strike-slip partitioned transpression and the formation and exhumation of eclogite facies rocks: an example from the Musgrave Block, central Australia. Tectonics 19, 978–996.
Camacho, A., Compston, W., McCulloch, M., McDougall, I., 1997. Timing and exhumation of eclogite facies shear zones, Musgrave Block, central Australia. J. Metamorph. Geol. 15 (6), 735–751.
Chakhmouradian, A.R., Wall, F., 2012. Rare earth elements: minerals, mines, magnets (and more). Elements 8 (5), 333–340.
Chassé, M., Griffin, W.L., O'Reilly, S.Y., Calas, G., 2016. Scandium speciation in a world-class lateritic deposit. Geochem. Perspect. 3 (2), 105–114.
Colin, F., Nahon, D., Trescases, J.J., Melfi, A.J., 1990. Lateritic weathering of pyroxenites at Niquelandia, Goias, Brazil; the supergene behavior of nickel. Econ. Geol. 85 (5), 1010–1023.
Davranche, M., Pourret, O., Gruau, G., Dia, A., Le Coz-Bouhnik, M., 2005. Adsorption of REE (III)-humate complexes onto MnO_2: Experimental evidence for cerium anomaly and lanthanide tetrad effect suppression. Geochim. Cosmochim. Acta 69 (20), 4825–4835.
Dublet, G., Juillot, F., Brest, J., Noel, V., Fritsch, E., Proux, O., Olivi, L., Ploquin, F., Morin, G., 2017. Vertical changes of the Co and Mn speciation along a lateritic regolith developed on peridotites (New Caledonia). Geochim. Cosmochim. Acta 217, 1–15.
Economou-Eliopoulos, M., Eliopoulos, D., Apostolikas, A., Maglaras, K., 1997. Precious and rare earth element distribution in Ni-laterites from Lokris area, Central Greece. In: Miner. Deposits. Balkema, Rotterdam, pp. 411–414.
Edgoose, C.J., Scrimgeour, I.R., Close, D.F., 2004. Geology of the Musgrave Block, Northern Territory. In: Northern Territory Geological Survey. Report 15.
Eliopoulos, D.G., Economou-Eliopoulos, M., 2000. Geochemical and mineralogical characteristics of Fe–Ni-and bauxitic-laterite deposits of Greece. Ore Geol. Rev. 16 (1–2), 41–58.
Frey, F.A., Haskin, M.A., Poetz, J.A., Haskin, L.A., 1968. Rare earth abundances in some basic rocks. J. Geophys. Res. 73 (18), 6085–6098.
Freyssinet, P., Butt, C.R.M., Morris, R.C., Piantone, P., 2005. Ore-forming processes related to lateritic weathering. In: Econ. Geol., 100th Anniversary, pp. 681–722.
Gleeson, S.A., Butt, C.R., Elias, M., 2003. Nickel laterites: a review. In: SEG Newsletter. SEG, pp. 54.
Golightly, J.P., 1981. Nickeliferous laterite deposits. In: Ec. Geol., 75th Anniversary, pp. 710–735.
Golightly, J.P., 2010. Progress in understanding the evolution of nickel laterites. In: SEG Special Publication. vol. 15. pp. 451–475.
Golightly, J.P., Arancibia, O.N., 1979. The chemical composition and infrared spectrum of nickel-and iron-substituted serpentine from a nickeliferous laterite profile, Soroako, Indonesia. Can. Mineral. 17 (4), 719–728.
Hand, M., Sandiford, M., 1999. Intraplate deformation in central Australia, the link between subsidence and fault reactivation. Tectonophysics 305 (1), 121–140.
Hoskins, D., Lemon, N., 1995. Tectonic development of the eastern Officer Basin, central Australia. Explor. Geophys. 26 (3), 395–402.
Howard, H.M., Smithies, R.H., Kirkland, C.L., Kelsey, D.E., Aitken, A., Wingate, M.T.D., Quentin De Gromard, R., Spaggiari, C.V., Maier, W.D., 2015. The burning heart—the Proterozoic geology and geological evolution of the west Musgrave Region, central Australia. Gondwana Res. 27 (1), 64–94.
Kalatha, S., Economou-Eliopoulos, M., 2015. Framboidal pyrite and bacterio-morphic

goethite at transitional zones between Fe–Ni-laterites and limestones: evidence from Lokris, Greece. Ore Geol. Rev. 65, 413–425.
Kapusta, J.P., 2006. Cobalt production and markets: a brief overview. JOM 58 (10), 33–36.
Laskou, M., Economou-Eliopoulos, M., 2007. The role of microorganisms on the mineralogical and geochemical characteristics of the Parnassos-Ghiona bauxite deposits, Greece. J. Geochem. Explor. 93 (2), 67–77.
Maier, W.D., Howard, H.M., Smithies, R.H., Yang, S., Barnes, S.J., O'Brien, H., Huhma, H., Gardoll, S.J., 2014. Mafic-ultramafic Intrusions of the Giles Event, Western Australia: Petrogenesis and Prospectivity for Magmatic Ore Deposits.
Maier, W.D., Howard, H.M., Smithies, R.H., Yang, S.H., Barnes, S.J., O'Brien, H., Huhma, H., Gardoll, S., 2015. Magmatic ore deposits in mafic–ultramafic intrusions of the Giles Event, Western Australia. Ore Geol. Rev. 71, 405–436.
Major, R.B., Conor, C.H.H., 1993. Musgrave block. In: The Geology of South Australia. vol. 1. pp. 156–167.
Mameli, P., Mongelli, G., Oggiano, G., Dinelli, E., 2007. Geological, geochemical and mineralogical features of some bauxite deposits from Nurra (Western Sardinia, Italy): insights on conditions of formation and parental affinity. Int. J. Earth Sci. 96 (5), 887–902.
McCollom, T.M., Seewald, J.S., 2013. Serpentinites, hydrogen, and life. Elements 9 (2), 129–134.
McDonough, W.F., Sun, S.S., 1995. The composition of the Earth. Chem. Geol. 120 (3–4), 223–253.
McKenzie, R.M., 1989. Manganese oxides and hydroxides. In: Minerals in Soil Environments, pp. 439–465.
McLennan, S.M., Hemming, S., McDaniel, D.K., Hanson, G.N., 1993. Geochemical approaches to sedimentation, provenance, and tectonics. In: Geol. S. Am. S. vol. 284. pp. 21–40.
Metals X Ltd, 2017. Annual report. https://www.metalsx.com.au/system/assets/109/original/Metals_X_2017_Annual_Report.pdf.
Mondillo, N., Balassone, G., Boni, M., Rollinson, G., 2011. Karst bauxites in the Campania Apennines (southern Italy): a new approach. Period. Mineral. 80, 407–432.
Mongelli, G., 1997. Ce-anomalies in the textural components of Upper Cretaceous karst bauxites from the Apulian carbonate platform (southern Italy). Chem. Geol. 140 (1–2), 69–79.
Mongelli, G., Boni, M., Buccione, R., Sinisi, R., 2014. Geochemistry of the Apulian karst bauxites (southern Italy): chemical fractionation and parental affinities. Ore Geol. Rev. 63, 9–21.
Mongelli, G., Sinisi, R., Mameli, P., Oggiano, G., 2015. Ce anomalies and trace element distribution in Sardinian lithiophorite-rich Mn concretions. J. Geochem. Explor. 153, 88–96.
Nahon, D., Colin, F., Tardy, Y., 1982. Formation and distribution of Mg, Fe, Mn-smectites in the first stages of the lateritic weathering of forsterite and tephroite. Clay Miner. 17 (3), 339–348.
Nesbitt, R.W., Goode, A.D.T., Moore, A.C., Hopwood, T.P., 1970. The Giles Complex, central Australia: a stratified sequence of mafic and ultramafic intrusions. In: Geological Society of South Africa Special Publication. vol. 1. pp. 547–564.
Pillans, B., Anand, R.R., de Broekert, P., 2005. Geochronology of the Australian regolith. In: Regolith-landscape Evolution Across Australia. CRC LEME Monographpp. 41–61.
Pirajno, F., Hoatson, D.M., 2012. A review of Australia's Large Igneous Provinces and associated mineral systems: implications for mantle dynamics through geological time. Ore Geol. Rev. 48, 2–54.
Pourret, O., Gruau, G., Dia, A., Davranche, M., Molenat, J., 2010. Colloidal control on the distribution of rare earth elements in shallow groundwaters. Aquat. Geochem. 16 (1), 31.
Putzolu, F., 2017. The Wingellina Ni-Co Laterite Project (West Musgrave Block, Western Australia). MSc thesis University of Naples, Italy, pp. 209.
Putzolu, F., Balassone, G., Boni, M., Maczurad, M., Mondillo, N., Najorka, J., Pirajno, F., 2018. Mineralogical association and Ni-Co deportment in the Wingellina oxide-type laterite deposit (Western Australia). Ore Geol. Rev. 97, 21–34.
Sun, S.S., Sheraton, J.W., Glikson, A.Y., Stewart, A.J., 1996. A major magmatic event during 1050–1080 in central Australia and an emplacement age for the Giles Complex. In: AGSO Research Newsletter. vol. 24. pp. 13–15.
Tardy, Y., Roquin, C., 1998. Derive des continents paleoclimats et altérations tropicales. Editions BRGM. (473 pp.).
Tauler, E., Lewis, J.F., Villanova-de-Benavent, C., Aiglsperger, T., Proenza, J.A., Domènech, C., Gallardo, T., Longo, F., Galí, S., 2017. Discovery of Ni-smectite-rich saprolite at Loma Ortega, Falcondo mining district (Dominican Republic): geochemistry and mineralogy of an unusual case of “hybrid hydrous Mg silicate–clay silicate” type Ni-laterite. Mineral. Deposita 52 (7), 1011–1030.
Vodyanitskii, Y.N., 2012. Geochemical fractionation of lanthanides in soils and rocks: a review of publications. Eurasian Soil Sci. 45 (1), 56–67.
Wade, B.P., Barovich, K., Hand, M., 2005. Towards a tectonic synthesis for the Musgrave Block. In: Hancock, H. (Ed.), STOMP 2005, Structure, Tectonics and Ore Mineralisation Processes (Abstract Volume), pp. 140.
Wade, B.P., Barovich, K.M., Hand, M., Scrimgeour, I.R., Close, D.F., 2006. Evidence for early Mesoproterozoic arc magmatism in the Musgrave Block, central Australia: implications for Proterozoic crustal growth and tectonic reconstructions of Australia. J. Geol. 114 (1), 43–63.
Walter, M.R., Veevers, J.J., Calver, C.R., Grey, K., 1995. Neoproterozoic stratigraphy of the centralian superbasin, Australia. Precambrian Res. 73 (1–4), 173–195.
Weill, D.F., Drake, M.J., 1973. Europium anomaly in plagioclase feldspar: experimental results and semiquantitative model. Science 180 (4090), 1059–1060.
Wingate, M.T.D., Pirajno, F., Morris, P.A., 2004. Warakurna large igneous province: a new Mesoproterozoic large igneous province in west-central Australia. Geology 32 (2), 105–108.